DEVELOPMENT OF A MID-INFRARED CARBON MONOXIDE SENSOR FOR A HIGH-PRESSURE COMBUSTOR RIG

A Thesis

by

JAMES PAUL ANDERSON

Submitted to the Office of Graduate and Professional Studies of
Texas A&M University
in partial fulfillment of the requirements for the degree of

MASTER OF SCIENCE

Chair of Committee,	Eric L. Petersen
Committee Members,	Waruna Kulatilaka
	Adonios N. Karpetis
Head of Department,	Andreas Polycarpou

May 2016

Major Subject: Mechanical Engineering

ABSTRACT

Carbon monoxide (CO) is a toxic byproduct of incomplete combustion in hydrocarbon-fueled systems which poses many environmental and human health hazards. Not only is CO hazardous, it also correlates to combustion efficiency. A mid-infrared (IR) CO detector has been developed to monitor the amount of CO produced by a high-pressure test rig developed by Parametric Solutions, Inc. under contract from Toshiba. The combustor rig was designed to operate using the Allam cycle, which requires methane and an oxygen/carbon dioxide blend, and operates at approximately 30MPa and 1150°C. The mid-IR system operates at the fundamental absorption band, $\nu'' = 0$, R(12), of CO near 4.5 µm. The mid-IR diagnostic was constructed from a tunable quantum cascade laser produced by Alpes Lasers, an absorption cell with two window ports for monitoring CO exhaust concentration, and two IR photodetectors. Temperature and pressure sensors were mounted near the absorption cell to monitor exhaust flow conditions, and the operational wavelength of the laser was determined by a calibration process using a known mixture of CO and N_2. Environmental conditions at the test facility posed significant difficulties in the data acquisition process for the IR diagnostic. Fluctuating environmental temperatures proved to be problematic when operating cryogenic photodetectors and stabilizing a quantum cascade laser designed to operate with an internal temperature of -15°C. Improvements to the IR system included elimination of problematic stagnation regions via a new absorption cell design, and an increase in the CO detection limit. During steady state conditions, the mid-IR diagnostic measured the CO concentration to be about 539.5 ± 80.6 ppm. It was discovered that during some of test runs, the CO absorption trace would be artificially raised due to unknown deposits on the inside of the cell windows. The IR diagnostic was shown to have superior CO detection response time and the ability to resolve features not detected by other CO detector counterparts.

ACKNOWLEDGMENTS

I would like to thank my advisor and committee chair, Dr. Eric Petersen for his guidance and support throughout my graduate career, giving me the opportunity to further my education, and allowing me to gain valuable experience working on large engineering projects. I would like to thank my co-workers and friends that helped throughout my work. Specifically I would like to thank Mathew Gill, Emiliano Vivanco, Anibal Morones, Clayton Mulvihill, Gabe Cruz, and Travis Sikes for offering their support and knowledge during my graduate experience.

NOMENCLATURE

Abbreviations

c	speed of light (m/s)
c_p	Specific heat (kJ/kg-K)
$\bar{c}_{p,i}$	Molar specific heat of species *i* (kJ/kmol-K)
G	Gibbs function (kJ)
G_T°	Standard-state Gibbs function (kJ)
G_{mix}	Total mixture Gibbs free energy (kJ)
$\bar{g}_{i,T}^{\circ}$	Gibbs of a pure species at standard state pressure (kJ/kmol)
g_j	Degeneracy of energy level *j*
h	Planck's constant (J s)
$\overline{h_{\iota}}$	Molar enthalpy of species i (kJ/kmol)
$\bar{h}_{f,i}^{\circ}$	Enthalpy of formation of species i (kJ/kmol)
$\bar{h}_{mix}$	Mixture enthalpy (kJ/kmol)
I	Molecular moment of inertia (kg m^2)
I_o	Incident intensity from IR detector (reference) (V)
I_t	Transmitted intensity from IR detector (transmitted) (V)
K_p	Equilibrium Constant
k	Boltzmann constant (m^2 kg s^{-2} K^{-1})
k_ν	Absorption coefficient (cm^{-1} atm^{-1})
L	Absorption path length (cm)

N_i	Number of moles of species i (kmol)
n_{ji}	Temperature coefficient
P	Pressure (kPa)
P°	Reference pressure (kPa)
P_i	Partial pressure of species *i* (kPa)
$Q(T)$	Partition function
R_u	Universal gas constant (kJ/kmol K)
$S(T)$	Absorption Linestrength (cm^{-2} atm^{-1})
T	Temperature (K)
s	Entropy (kJ/kg K)
$\overline{s_\iota}$	Molar entropy of species i (kJ/kmol-K)
$\bar{s}_{mix}$	Mixture entropy (kJ/kmol-K)
T_{ref}	Reference temperature (K)
X_i	Mole fraction of species i

Greek Symbols

α_ν	Absorbance at wavenumber ν
$\Delta\nu_c$	Collisional linewidth
$\Delta\nu_D$	Doppler linewidth
ϕ_C	Lorentzian lineshape function
ϕ_D	Doppler lineshape function
ϕ_ν	Voigt lineshape function

ε_j	Molecular energy at level j
ε'	Total molecular energy
ν	Wavenumber (cm^{-1})
ν_o	Center wavenumber of molecular transition (cm^{-1})
γ_{ji}	Broadening coefficient of j with i

TABLE OF CONTENTS

Page

LIST OF FIGURES

LIST OF TABLES

Page

1. INTRODUCTION

1.1 Motivation and Scope

Carbon Monoxide (CO) is a toxic byproduct of incomplete combustion in hydrocarbon-fueled systems that posts many environmental and human health hazards. Not only does CO pose a health hazard, it is also correlates to the efficiency of the combustion process. For example, the fuel-air mixture of a combustor is often for simplicity taken to be homogenous throughout the entire volume of the combustion chamber. In reality, combustion systems can contain discrete combustion zones and areas of non-homogenous mixture. This inhomogeneity can cause fuel-rich regions, leading to CO production due to lack of oxygen to produce carbon dioxide (CO_2). Thus, CO is an important parameter to measure during combustor operation as it provides important information on the combustion efficiency of the system. The concentration measurement method of interest herein utilizes laser absorption of CO.

Laser absorption Spectroscopy has played a large and expanding role in the measurement of many combustion parameters such as temperature, pressure, velocity, and gas composition. The utilization of laser absorption spectroscopy has gained popularity due to its ability to perform time sensitive, non-intrusive, *in situ* measurements. Several groups have studied infrared CO absorption transitions near 1.55, 2.3, and 4.5-μm wavelengths.[1-13] A major consideration when choosing an operational wavelength for an absorption spectroscopy measurement is the absorption linestrength of the target species versus the absorption linestrengths of interfering species. For this thesis, it was important to choose a wavelength of substantial linestrength for CO while simultaneously minimizing interference from other combustion products such as CO_2, H_2O, and O_2.

As part of a new natural gas powered cycle, Toshiba contracted Parametric Solutions Incorporated (PSI) to construct the Zeus combustor test rig. Due to the high pressure nature of the experiment, and the physical location of the combustor, the ability to accurately acquire CO measurements with the mid-IR diagnostic proved to be difficult. The combustor rig test facility was located at the National Technical Systems (NTS) facility in San Bernardino, CA. During the summer the local temperature at the NTS facility could fluctuate up to 50°F during the day. This posed a significant strain on the cryogenically cooled IR photodetectors, and on the cooling systems of the quantum cascade laser such that a secondary cooling system had to be installed. Remote monitoring of the IR system was necessary due to the extreme pressures rig operation pressures and the location of the IR diagnostic to the combustor rig. More information on the experimental setup is located in section 3.

The scope of this thesis was focused on the improvement and operation of mid-IR sensors for time-sensitive CO measurements with an operational wavelength around 4.5 μm using tunable diode laser absorption spectroscopy. The mid-IR absorption CO sensor was applied to a high-pressure industrial combustor test rig to measure the CO emissions during operation. The first generation of the measurement system in the present high-pressure combustor application was established in 2014 in the thesis work by Camou[14]. The present CO measurements were performed using a tunable diode laser from Alpes Lasers by applying the principles of direct absorption spectroscopy. The mid-IR diagnostic was placed close to the combustor rig to ensure fast response time between changing combustor conditions and detection of the resultant CO profile, and one of the primary challenges to be solved in this thesis was the successful demonstration of the diagnostic in the difficult environment of a live combustor firing.

1.2 Organization of Thesis

The present section discussed the motivation, scope and objective of the mid-IR CO diagnostic. Section 2 provides background theory in combustion chemistry and absorption spectroscopy. Section 3 discusses the mid-IR diagnostic equipment, the absorption cell and cell improvements, an overview of the combustor rig, and other emissions diagnostics. Section 4 highlights the mid-IR calibration procedure and remote monitoring equipment. Section 5 discusses the Data analysis procedure and MATlab code. Section 6 provides results and discussion and section 7 provides recommendations and improvements.

2. BACKGROUND

This section introduces scientific theories that are used in this thesis and presents general equations. First, the basic underlying principles of equilibrium combustion chemistry are presented, followed by topics pertaining to hydrocarbon combustion, combustion byproducts, and equilibrium exhaust product formation. The second subsection discusses topics pertaining to laser absorption spectroscopy, the Beer-Lambert law, energy partition functions, and rotational-vibrational spectroscopy with a focus toward the CO molecule and compositional measurement.

2.1 Equilibrium Combustion Chemistry

To develop the concept of chemical equilibrium, this section starts with the definitions of entropy and enthalpy for an ideal gas. Using the developed relations, the Gibbs function are defined and related to the chemical equilibrium constant for a general chemical reaction. During the process of combustion, the exhaust species depend on several factors such as flame temperature, chamber pressure, fuel-to-air ratio, and the fuel and air composition. Equation 1 defines the entropy change of an ideal gas.[15]

$$ds = c_p \frac{dT}{T} - R_u \frac{dP}{P} \tag{1}$$

Where the change in entropy is ds, c_p is the specific heat at constant pressure, T is the temperature, R_u is the universal ideal gas constant, and P is pressure. This relation can be manipulated to a more useful form using the following two equations:

$$d\bar{s_i} = \bar{s_i}(T, P) - \bar{s_i}\left(T_{ref}, P^{\circ}\right) = \bar{s_i}^{\circ}(T) - R_u \ln\left(\frac{P_i}{P^{\circ}}\right) \tag{2}$$

$$\overline{s_i}^{\circ}(T) = \int_{T_{ref}}^{T} \bar{c}_{p,i} \frac{dT}{T} \tag{3}$$

where $\overline{s_i}^{\circ}$ is the entropy of formation for species i on a per mole basis, and P_i is the partial pressure of species i. The values of P° and T_{ref} are generally taken to be 1 atm and 298 K, respectively. This approach can be extended to define the specific entropy of a mixture of ideal gases by summing the specific entropies of each component multiplied by the mole fraction of that component.

$$\bar{s}_{mix}(T,P) = \sum X_i \overline{s_i} \tag{4}$$

Using similar methods, the specific enthalpy of the mixture is defined as:

$$\bar{h}_{mix}(T,P) = \sum X_i \overline{h_i} \tag{5}$$

where X_i is the mole fraction of species i, and $\bar{h}_i$ is the molar specific enthalpy. The species-specific enthalpy is defined as:

$$\overline{h_i}(T) = \bar{h}_{f,i}^{\circ} + \int_{T_{ref}}^{T} \bar{c}_{p,i} dT \tag{6}$$

where $\int_{T_{ref}}^{T} \bar{c}_{p,i} dT$ makes up the sensible enthalpy, and $\bar{h}_{f,i}^{\circ}$ is the enthalpy of formation for species i.

While the definition of entropy is important for showing how the Second Law applies to equilibrium chemistry, using enthalpy and entropy we can define a new state function, the Gibbs free energy, as defined by the following:

$$G = H - TS \tag{7}$$

The Gibbs function for a mixture of ideal gases can be expressed as follows:

$$G_{mix} = \sum N_i \bar{g}_{i,T} = \sum N_i \left[\bar{g}^{\circ}_{i,T} + R_u T ln \left(\frac{P_i}{P^{\circ}} \right) \right] \tag{8}$$

where N_i is the number moles of species i, and $\bar{g}^{\circ}_{i,T}$ is the Gibbs function of a pure species at standard state pressure.

Equation 9 shows a general chemical reaction

$$aA + bB \leftrightarrow \mathrm{dD} + \mathrm{eE} \tag{9}$$

For this general reaction, the equilibrium constant K_p can be defined as the following:

$$K_p = \frac{\left(\frac{P_D}{P^{\circ}}\right)^d \left(\frac{P_E}{P^{\circ}}\right)^e}{\left(\frac{P_A}{P^{\circ}}\right)^a \left(\frac{P_B}{P^{\circ}}\right)^b} = \frac{(X_D)^d (X_E)^e}{(X_A)^a (X_B)^b} \tag{10}$$

The equilibrium constant is a vital parameter to combustion chemistry, and it is used to determine equilibrium mole fractions for chemical reactions operating at a given condition. Changes in the Gibbs function can be related to K_p using the following expressions:

$$\Delta G^{\circ}_T = -R_u T ln\left(K_p\right) \tag{11}$$

$$K_p = \exp\left(\frac{-\Delta G^{\circ}_T}{R_u T} \right) \tag{12}$$

Replacing K_p with its definition yields the following result:

$$\frac{(X_D)^d (X_E)^e}{(X_A)^a (X_B)^b} = \exp\left(\frac{-\Delta G_T^{\circ}}{R_u T}\right) \tag{13}$$

The equation above is useful because it can relate equilibrium concentrations of several species to the Gibbs function. To fully solve for the amount of each species present at equilibrium, other methods must be implemented, such as performing a conservation of elements and assuring that the sum of all mole fractions is equal to unity.

2.2 Laser Absorption Spectroscopy

This section defines concepts used in direct laser absorption spectroscopy. The next subsections focus on definitions pertaining to spectral line broadening and the effect it has on the spectral lineshape, background physics and concepts relating to species measurement using the Beer Lambert Law, and an introduction into rotational-vibrational spectroscopy.

2.2.1 Spectral Broadening and Lineshape

Quantum transitions between energy levels in atoms and molecules are not infinitely sharp, i.e., not purely monochromatic.[16] Spectral lines not only have some associated shape and distribution that is associated with frequency, but mechanisms exist that perturb the lineshape. The two main mechanisms that are focused on herein are collisional broadening and Doppler broadening. The convolution of these two broadening mechanics forms the spectral lineshape known as the Voigt profile. Other broadening mechanisms exists, but are not explored further in this thesis[16]. Figure 1 shows normalized Lorentzian and Gaussian profiles.

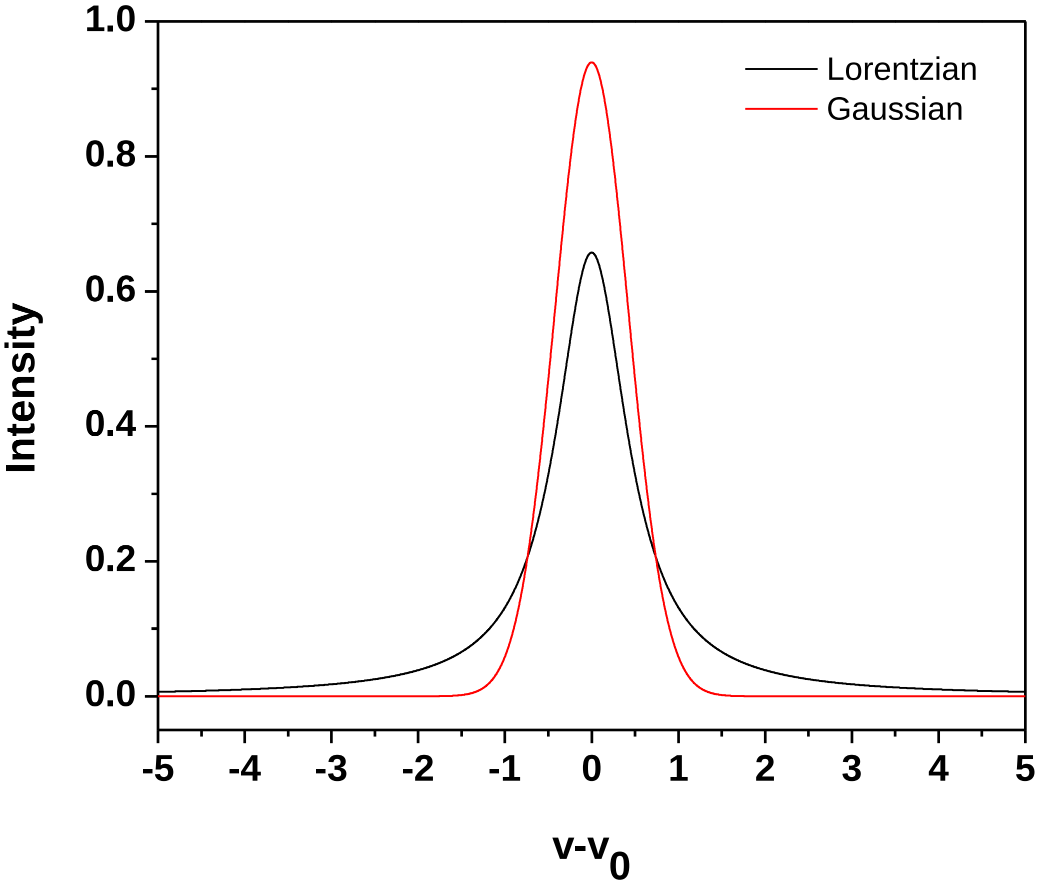

Figure 1: Examples of Lorentzian and Gaussian profiles

Collisional, or pressure, broadening arises from energy shifts induced by particle-particle interactions and will cause the lineshape to broaden and the line-center to shift in frequency. The collisional broadening lineshape function results in a Lorentzian profile and is described by the following equation:

$$\phi_C(\nu) = \frac{\Delta\nu_c/_2}{\pi\left[(\nu - \nu_o)^2 + \left(\Delta\nu_c/_2\right)^2\right]} \tag{14}$$

where ϕ_C is the collisional broadening lineshape function, ν_o is the central frequency, $\Delta\nu_s$ is the shift in the line-center, and $\Delta\nu_c$ is the Full Width at Half Maximum (FWHM). The FWHM of the function is described by equation 15.

$$\Delta\nu_c = P\sum_j X_j 2\gamma_{ji} \tag{15}$$

Where P is the total pressure, X_j is the mole fraction of collisional partner of the measured species i, and γ_{ji} is the is the broadening coefficient of j with i. The broadening coefficient can be tabulated as a temperature dependent function as shown below,

$$\gamma_{ji} = \gamma_{ji}(T_o)\left(\frac{T_o}{T}\right)^{n_{ji}} \tag{16}$$

where T_o is a reference temperature, and n_{ji} is the temperature coefficient.

Doppler broadening arises from thermal motion of atoms or molecules and causes a shift in the central frequency. When an absorbing molecule is moving in the direction of propagation of the laser source a frequency shift is induced. The Doppler lineshape function results in a Gaussian profile and is described by the following equation:

$$\phi_D(\nu) = \frac{2}{\Delta\nu_D}\sqrt{\frac{ln2}{\pi}}\exp\left[-4ln2\left(\frac{\nu-\nu_o}{\Delta\nu_D}\right)^2\right] \tag{17}$$

Where $\Delta\nu_D$ is the Doppler linewidth, defined by the following:

$$\Delta\nu_D = \frac{2\nu_o}{c}\sqrt{\frac{2\ln(2)\,kT}{m}} \tag{18}$$

Where k is Boltzmann’s constant, c is the speed of light, and m is the molecular weight of the absorbing species.

At low pressures, Doppler effects dominate broadening parameters while collisional effects dominate at high pressures. At conditions where neither Doppler nor collision broadening dominates, the two effects combine to give a lineshape described by the Voigt profile.[16]It is important to capture both effects of Doppler and collision broadening when analyzing the spectra at a given transition, thus the Voigt profile has great use. The Voigt profile is defined as follows:

$$\phi_V(\nu) = 2\sqrt{\frac{ln2}{\pi}}\frac{V(a,x)}{\Delta\nu_D} \tag{19}$$

where $V(a,x)$ is the normalized Voigt function of two dimensionless variables a and x.

$$V(a,x) = \frac{a}{\pi}\int_{-\infty}^{\infty}\frac{e^{y^2}}{a^2+(x-y)^2}dy \tag{20}$$

$$x = 2\sqrt{ln2}\frac{(\nu - \nu_o)}{\Delta\nu_D} \tag{21}$$

$$a = \sqrt{ln2}\frac{\Delta\nu_c}{\Delta\nu_D} \tag{22}$$

2.2.2 Beer-Lambert Law

The Beer-Lambert Law is an extremely useful principle that is used in absorption spectroscopy for measuring species concentration in a gas. The Beer-Lambert law utilizes the fractional attenuation of monochromatic light at frequency ν through a uniform medium to determine the fractional composition of the species in question. Figure 2 shows a simplified schematic for direct absorption spectroscopy measurements.

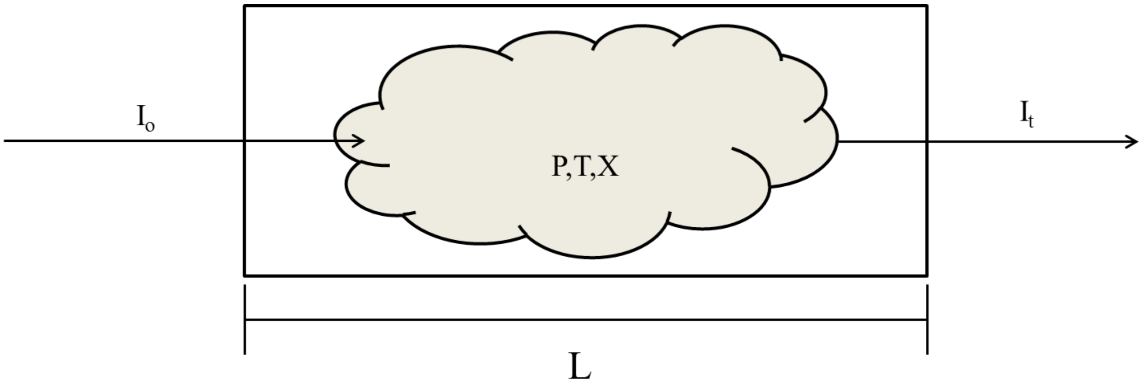

Figure 2: A simplified diagram of an absorption spectroscopy setup. The absorbance path length, L, is the distance the laser travels through the medium.

The relation is defined as follows:

$$\left(\frac{I_t}{I_o}\right) = \exp(-\alpha_\nu) \tag{23}$$

where I_t is the transmitted light after leaving the medium, I_o is the incident light before entering the medium, and α_ν is the spectral absorbance of the absorbing species. The spectral absorbance is dependent on several factors: distance the light travels through the medium, pressure, the Voigt line-shape function, mole fraction of the absorbing species, and the absorption line strength. The spectral absorbance is defined as:

$$\alpha_\nu = PX_iS(T)_i\phi_\nu L \tag{24}$$

where P is the pressure, X_i is the mole fraction of the absorbing species, $S(T)_i$ is the absorption line strength of the absorbing species, and L is the length of the path the light takes passing through the medium. In most cases, the pressure, temperature, and absorption path length are known quantities. By using the fractional attenuation of the monochromatic light, the mole fraction of the absorbing species can be solved for. While the previously stated parameters can be directly measured, the absorption line strength and Voigt lineshape function must be calculated. These two parameters are grouped together and are referred to as the absorption coefficient, defined as:

$$k_\nu(T,P) = S(T)_i\phi_\nu \tag{25}$$

The absorption line strength is defined as:

$$S(T) = S(T_o)\frac{Q(T_o)}{Q(T)}\left(\frac{T_o}{T}\right)\exp\left[-\frac{hcE''}{k}\left(\frac{1}{T}-\frac{1}{T_o}\right)\right]\frac{\left[1-\exp\left(\frac{-hc\nu_o}{kT}\right)\right]}{\left[1-\exp\left(\frac{-hc\nu_o}{kT_o}\right)\right]} \tag{26}$$

where $Q(T)$ is the partition function, E'' is the lower-state energy, and h is Planck's constant.

2.2.3 Partition Functions

The partition function arises as a consequence of quantum mechanics. In quantum mechanics, energy modes may only occur at discrete values. When observing an ensemble of particles, a number of energy states, or macro states, are possible, causing the more probable macro states to have a higher population. The most probable macro state is the state that contains the greatest number of micro states. While each micro state is equally probable, some macro states contain more micro states depending on the thermodynamic conditions of the system. The number of micro states per macro state is known as the degeneracy of that state. The population distribution of macro states is described by the partition function and is defined as

$$Q(T) = \sum_j g_j e^{-\varepsilon_j/kT} \tag{27}$$

where g_j is the degeneracy of energy level j, and ε_j is the molecular energy at level j. The total energy of a molecule is defined as the sum of its translational, rotational, vibrational, and electronic energies:

$$\varepsilon' = \varepsilon'_{tans} + \varepsilon'_{rot} + \varepsilon'_{vib} + \varepsilon'_{el} \tag{28}$$

For any particle, there is a minimum amount of energy that can be obtained known as the zero point energy, ε_o, which is achieved at 0 kelvin. Thus we can define the total energy as:

$$\varepsilon' = \varepsilon_{trans} + \varepsilon_{rot} + \varepsilon_{vib} + \varepsilon_{el} + \varepsilon_o \qquad (29)$$

It can also be shown that the total energy above the zero point is:

$$\varepsilon = \varepsilon' - \varepsilon_o = \varepsilon_{trans} + \varepsilon_{rot} + \varepsilon_{vib} + \varepsilon_{el} \qquad (30)$$

It is also known from quantum mechanics, and assuming that the zero point energy is small, that the fallowing equalities are true [17]:

$$\varepsilon_{trans} \approx \frac{h^2}{8m}\left(\frac{n_1^2}{a_1^2} + \frac{n_2^2}{a_2^2} + \frac{n_3^2}{a_3^2}\right) \qquad (31)$$

$$\varepsilon_{rot} \approx \frac{h^2}{8\pi^2 I} J(J+1) \qquad (32)$$

$$\varepsilon_{vib} \approx vh\nu \qquad (33)$$

$$\varepsilon_{el} \approx \varepsilon'_{el} \qquad (34)$$

Where n is a translational quantum number, v is the vibrational quantum number, J is the rotational quantum number, and I is the moment of inertia of the molecule. Thus using equation 27, it can be shown that the total partition function is the product of each individual partition function:

$$Q(T) = \left[\sum_i g_i e^{-\frac{\varepsilon_{i_{trans}}}{kT}}\right]\left[\sum_j g_j e^{-\frac{\varepsilon_{j_{rot}}}{kT}}\right]\left[\sum_n g_n e^{-\frac{\varepsilon_{j_{vib}}}{kT}}\right]\left[\sum_l g_l e^{-\frac{\varepsilon_{l_{el}}}{kT}}\right] \qquad (35)$$

or

$$Q(T) = Q(T)_{trans} Q(T)_{rot} Q(T)_{vib} Q(T)_{el} \qquad (36)$$

For a more in depth derivation and explanation, see Anderson.[17]

2.2.4 Rotational-Vibrational Spectroscopy and the CO Molecule

This subsection discusses the fundamentals of Rotational-vibrational spectroscopy and how it applies to the exact energy transition being monitored in this thesis. Rotational-vibrational spectroscopy is of interest in combustion applications for a number of reasons, including *in situ* measurements via absorption spectroscopy.[16]

Rotational-vibrational spectroscopy primarily operates in the infrared or near infrared region of the electromagnetic spectrum. As stated in the previous section, the partition function is dependent on the quantum transitions of the molecule in question. Figure 3 shows rotational (J) and vibrational (ν) transitions occurring in the electronic ground state.[16] [18]

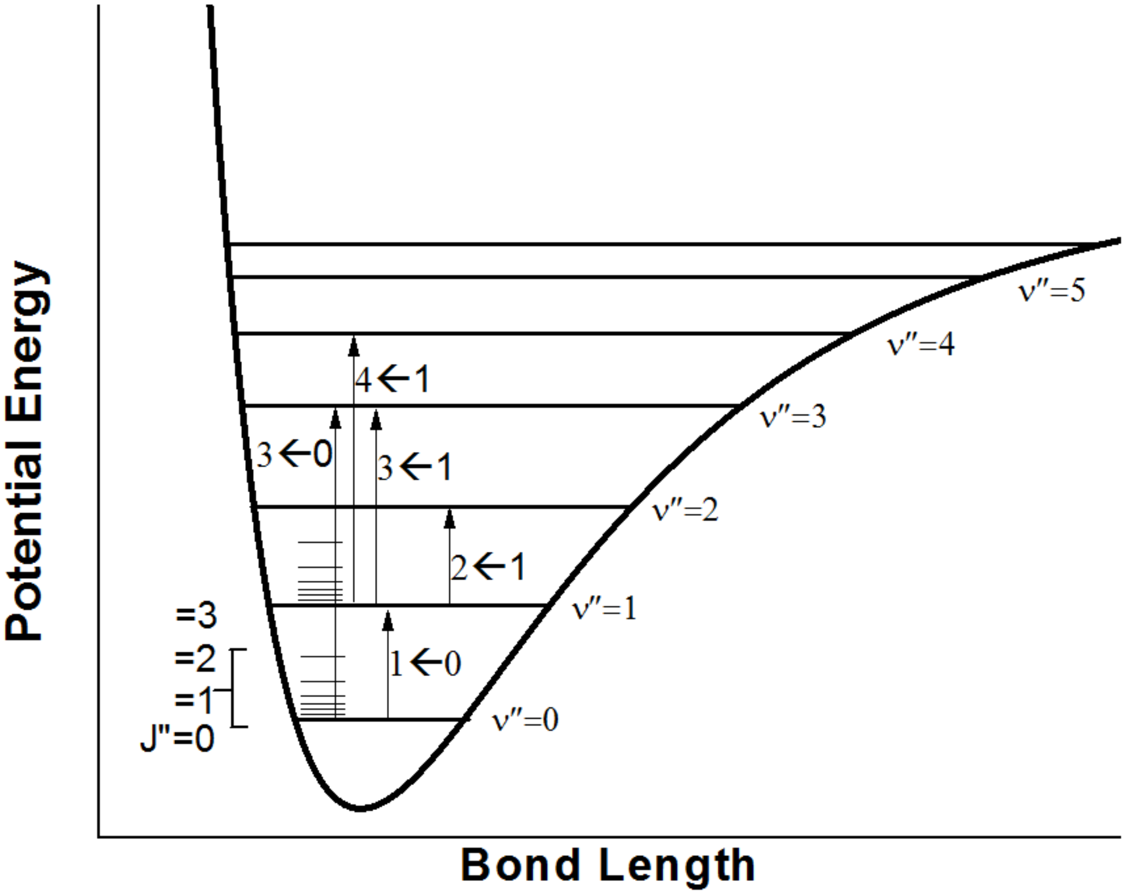

Figure 3: Potential energy curve and energy levels for a diatomic molecule in the electronic ground state

Derived from quantum mechanics are selection rules describing which transitions are allowed to take place and which transitions are forbidden. For the vibrational quantum number ν, the transitions allowed are $\Delta\nu = \pm1, \pm2, \pm3, \ldots$, while for a rotational transition the allowed change in quantum number is $\Delta J = 0, \pm1$. For CO, the transition $\Delta J = 0$ is forbidden, meaning a pure vibrational transition is not allowed. For rotational-vibrational transitions where $\Delta J = 1$, this is referred to as the R branch, $\Delta J = -1$ the P branch, and $\Delta J = 0$ the Q branch. To denote exactly which transition is being mentioned, the vibrational quantum number is listed followed by the branch letter and notated by the lower rotation transition, for example, in this paper the CO transition being targeted is the $\nu'' = 0$, R(12).

The reason the $\nu'' = 0$, R(12) transition was chosen for CO near 4.5 µm was due to its significantly higher absorption line strengths compared to other CO absorption bands. In addition to higher line-strengths, the absorption line is magnitudes stronger than the interfering combustion products such as H_2O and CO_2 near the 4.5 µm region. [1] For analysis of the absorption line strengths of the combustion products, the HITRAN database was used; a more in-depth discussion is contained in section 5 of this thesis. Figures 4-6 show absorption line strengths from 3-6 µm for CO, CO_2, and H_2O respectively.

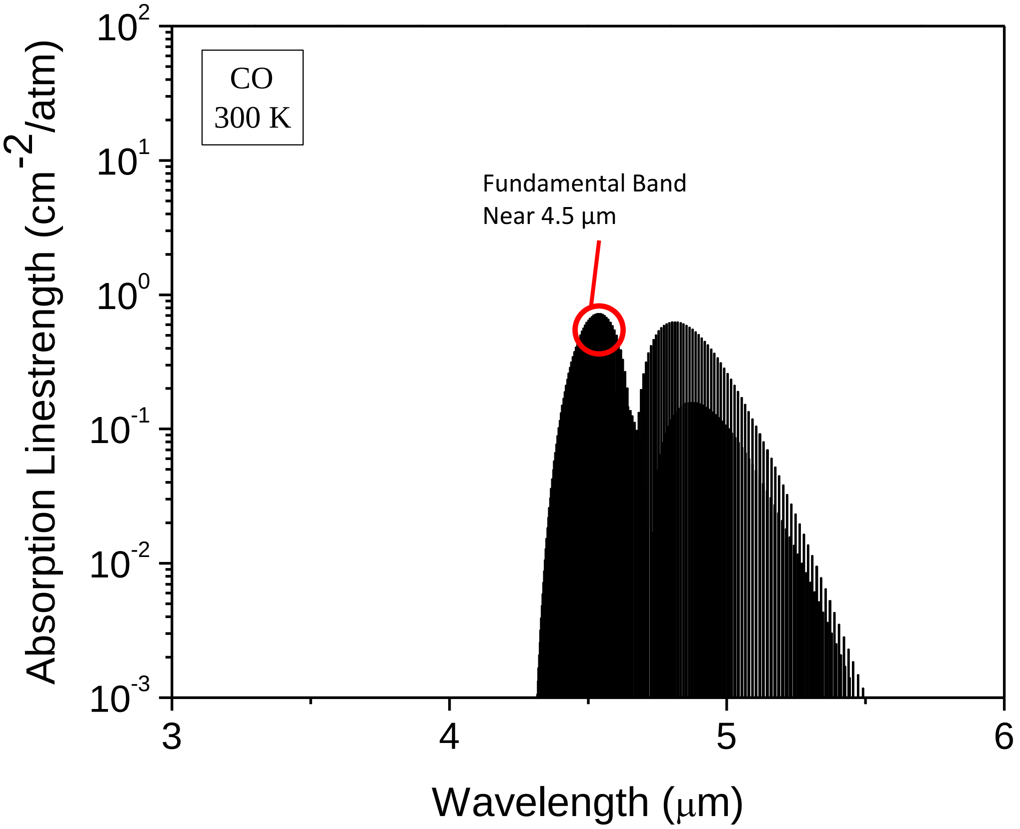

Figure 4: CO absorption linestrength from 3-6 μm, obtained from HITRAN.

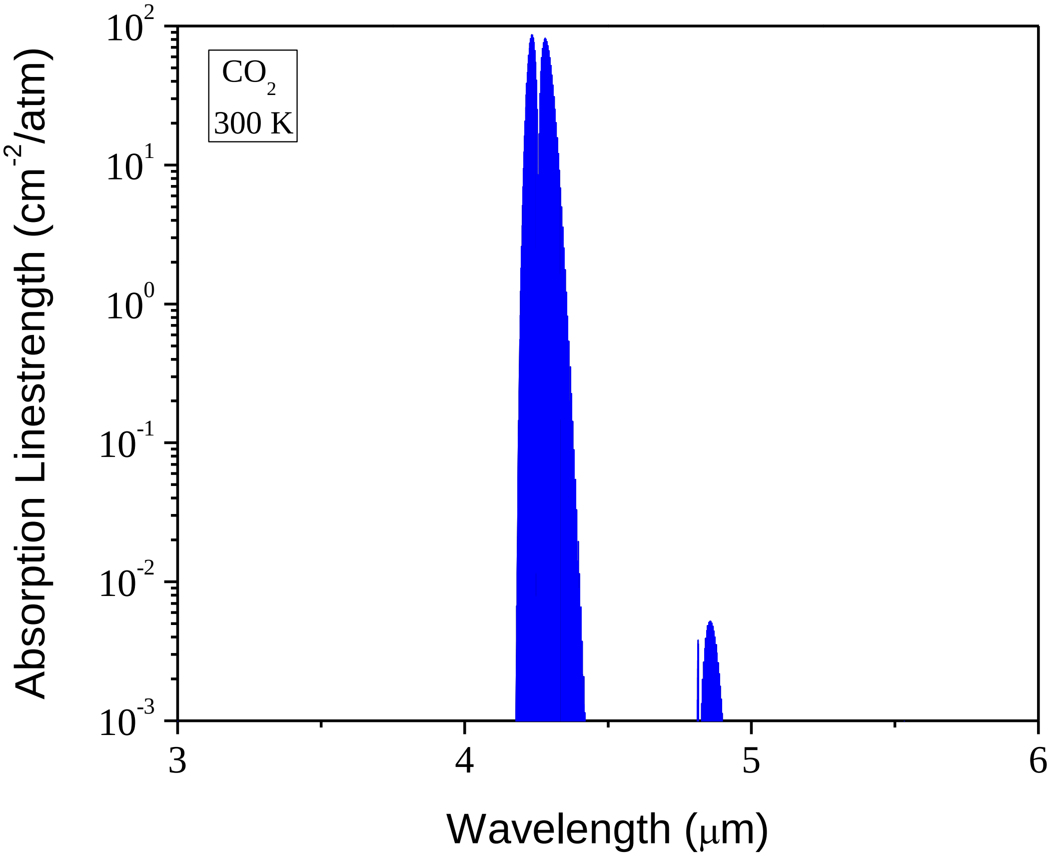

Figure 5: CO_2 absorption linestrength from 3 - 6 μm, per the HITRAN database.

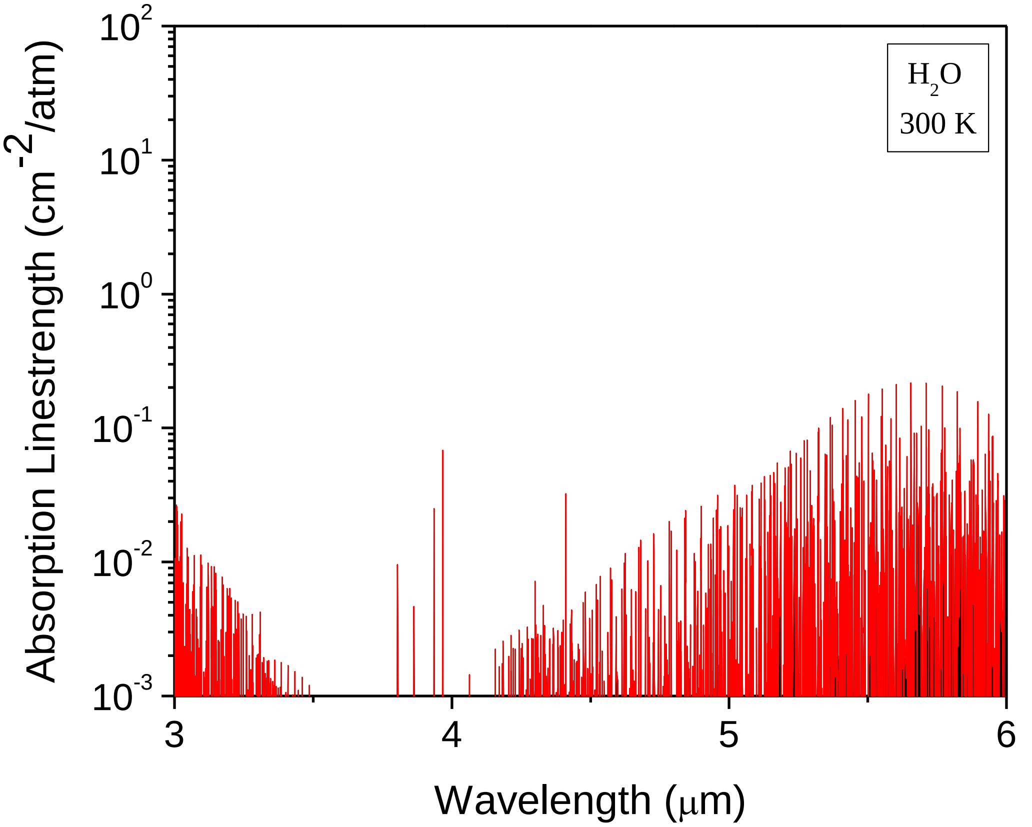

Figure 6: H_2O absorption linestrength from 3 -6 μm, per the HITRAN database.

3. EXPERIMENTAL SETUP

The primary objective of the Zeus combustor performance tests was to show stable combustion at target conditions using a mixture of methane, oxygen, and carbon dioxide. Prior to the continuation of the Texas A&M University's involvement with CO emission analysis, the mid-IR CO detector was developed and validated using shock-heated mixtures of known composition.[14] Further details on the combustion and cycle aspects of the combustor are mostly proprietary but are briefly summarized in [19]. This chapter discusses the experimental setup for the mid-IR CO detector system and some improvements that had been implemented as part of this thesis during the continuation of combustor rig performance tests.

3.1 Mid-IR Equipment

3.1.1 Quantum Cascade Laser

The Quantum Cascade Laser (QCL) produced by Alpes Lasers is a continuous-wave, distributed-feedback (CW-DFB) diode laser that was chosen for its operational wavelength and due to its ability to function in non-ideal laboratory environments without the need for cryonics.

The QCL was driven by a LDX-3232 current controller and TC-3 temperature controller from Alpes Lasers. The laser was thermoelectrically cooled to an operational temperature of -15 °C and sourced with 400 mA of current to achieve an operational wavelength near 2190.02 cm^{-1}, correlating to the $\nu''=0$, R(12) transition of the CO molecule. Developments in QCL technology have led to broad applications in detection of trace gases, due to room-temperature operation, narrow line-width, and signal-to-noise improvements.[1]

3.1.2 InSb Detectors

The mid-IR detector selection was based on the desired operational wavelength of the QCL at 2190.02 cm^{-1}. It was found that a pair of Indium Antimonide (InSb) photodiodes from Teledyne Judson Technologies would offer the highest signal-to-noise at the given wavelength. The InSb photodiodes generate a current when exposed to IR radiation and must be cooled with liquid nitrogen to decrease the number of thermal electrons causing a dark current in the semiconductor. As a consequence, the InSb photodiodes have a high sensitivity to changing environmental temperatures causing the zero-signal voltage to increase with rising temperatures.

A pair of PA-9 preamplifiers was connected to the output of the InSb detectors, with a maximum output of -10 volts and a bandwidth of 1 MHz for time-sensitive measurements.

3.1.3 Optics and Mirrors

All optics selected were designed for optimal performance at a wavelength of 2190.02 cm^{-1}. The optical layout consisted of 1-inch diameter gold-coated mirrors, a Calcium Floride (CaF_2) 50/50 beam splitter, two CaF_2 focusing lenses, two IR polarizers, a set of bandpass filters centered at 4.5 μm, and a pair of irises used to help isolate the photodiodes from surrounding IR radiation. Figure 7 shows a simplified schematic for the mid-IR CO diagnostic.

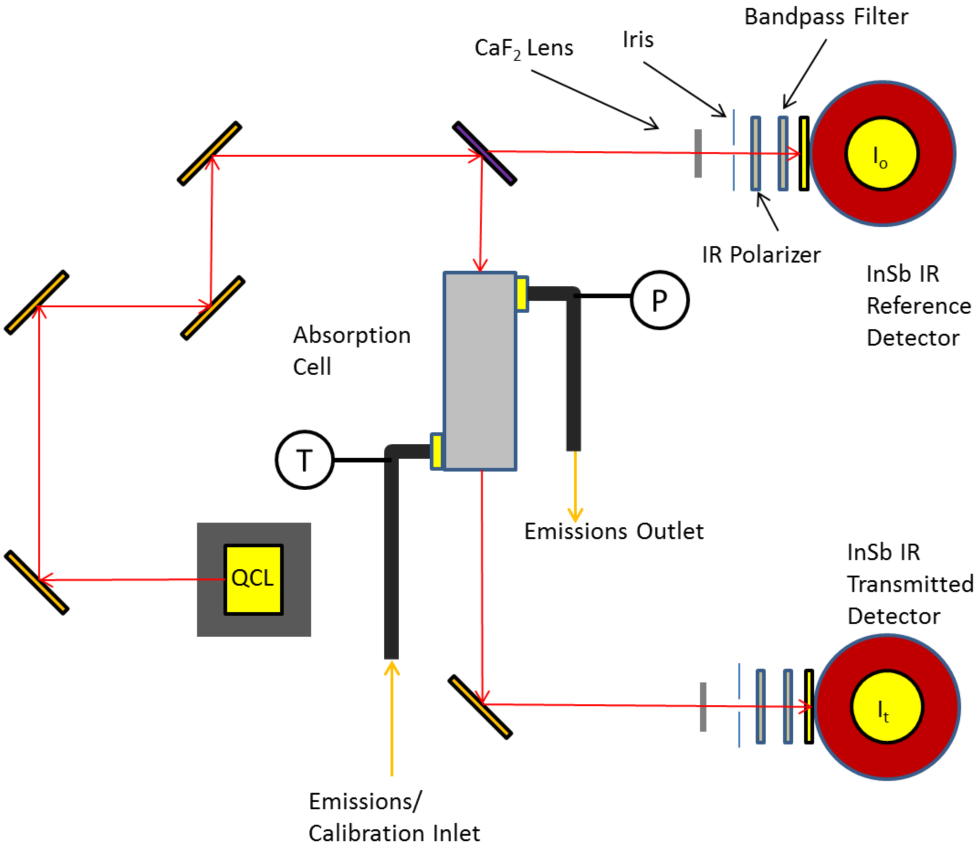

Figure 7: Mid-IR diagnostic setup

3.2 Absorption Cell

In the Beer-Lambert law, monochromatic light must have a way to interact with the sample being measured. For the mid IR setup, this was accomplished by having a cell of small volume with window ports to allow the IR beam from the QCL to pass through. Although the cell design went through revisions, the fundamental design remained the same. The absorption cell consisted of translucent windows at 4.5 μm, a pressure transducer and thermocouple to record thermodynamic conditions within the absorption cell. This subsection describes in detail the functionality, issues, and revisions of each IR absorption cell.

3.2.1 The Original Cell

The original cell, as seen in Fig. 8, was a simple, tee-based design that had a minimal volume with the beam path perpendicular to the sample flow with a beam path length of 11.8 cm, allowing for a maximum CO reading of approximately 20,000 parts per million (ppm), or 2%. The view ports consisted of 1.5-mm diameter sapphire windows attached via Swagelok fittings to the body of the cell.

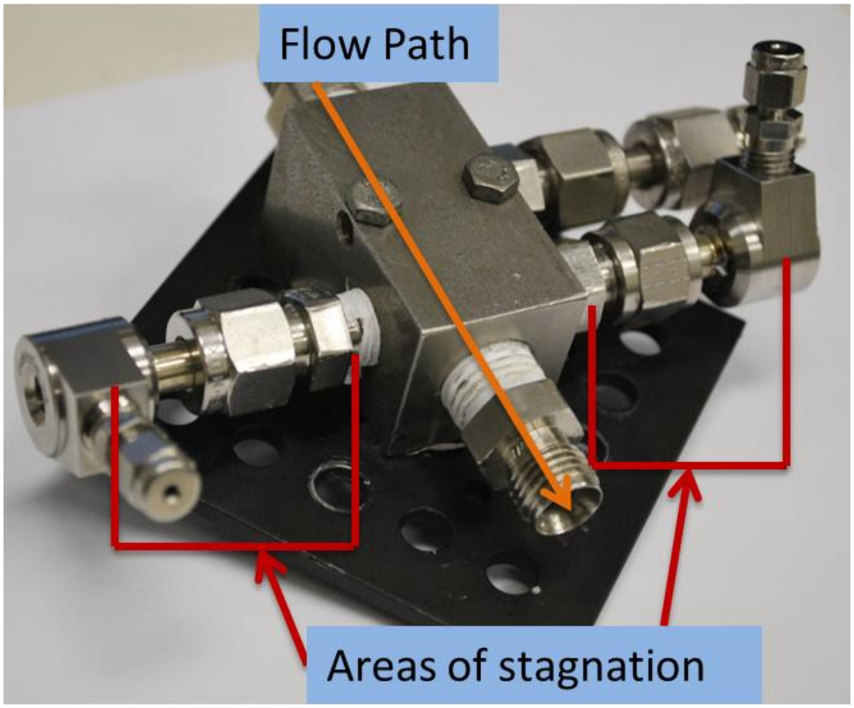

Figure 8: Original test cell design. Areas of the absorption cell thought to have slow clearance times, causing poor response in detector.

While this cell was a valid first step in the design of the mid IR CO detector, it was not without flaw. One issue presented was a noticeably longer residence time than with its turnkey CO-measuring counterparts provided by California Analytical Instruments (CAI). (See section 3.4 for more information on the CAI gas analyzer). Figure 9 show the CO profiles gather from the mid-IR system and the CAI analyzer: EM1 and EM2.

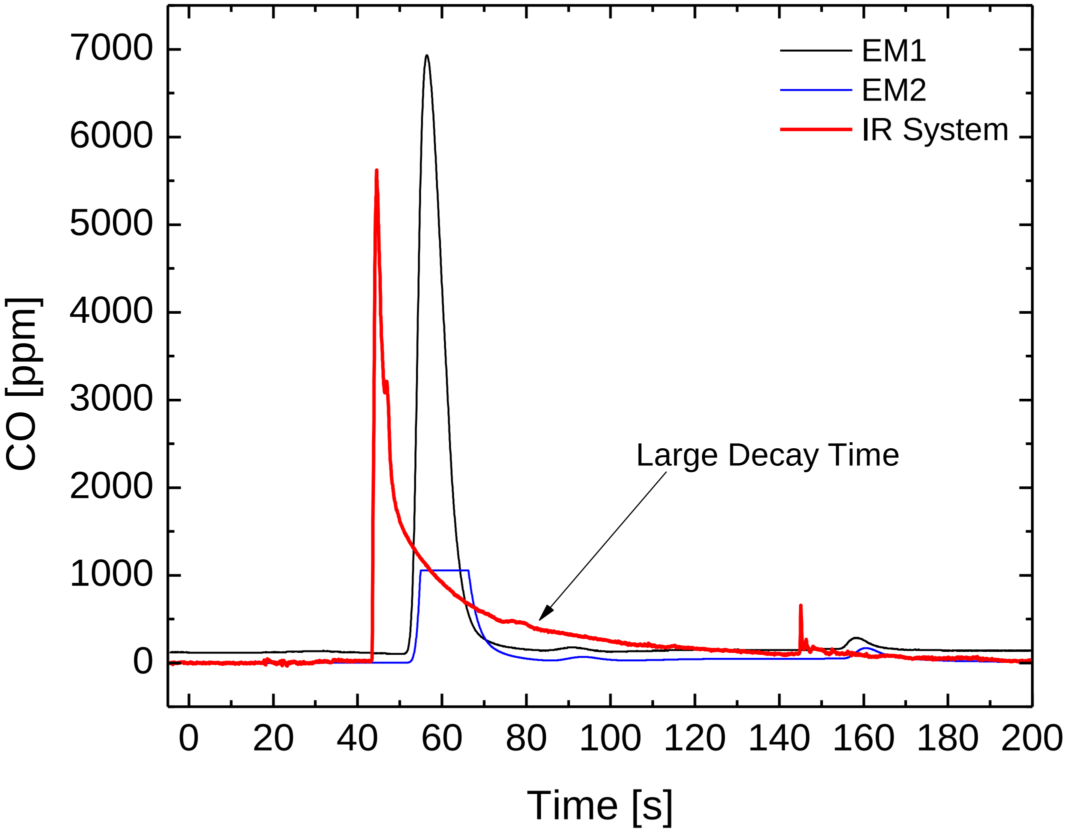

Figure 9: Depiction of large decay time present in original absorption cell design during hot-fire test HF-97. EM1 and EM2 are measurements of the CAI analyzer

As seen in Fig. 9, the 4.5-μm IR system takes nearly 6 times as long to reach a steady state value after the ignition event near 40 seconds, than CAI analyzers EM1 and EM2. This was believed to be caused by stagnation of combustion gases occurring within the cell; these stagnation zones were not able to flush out due to the small-volume, tee-shaped design (Fig. 8). To solve this issue, a new laser absorption cell was commissioned as a part of this thesis.

3.2.2 New Absorption Cell

When designing the new laser absorption cell, a set of parameters had to be considered to maintain functionality while improving on the residence time of the previous design. The new cell was initially designed to maintain the same optical path length and therefore to have the same CO detection limits as the previous design while having a minimization of volume and subsequent improvement of the detector residence time. Figure 10 shows the new absorption cell with a coaxial design, causing the laser beam path to be parallel with the sample flow.

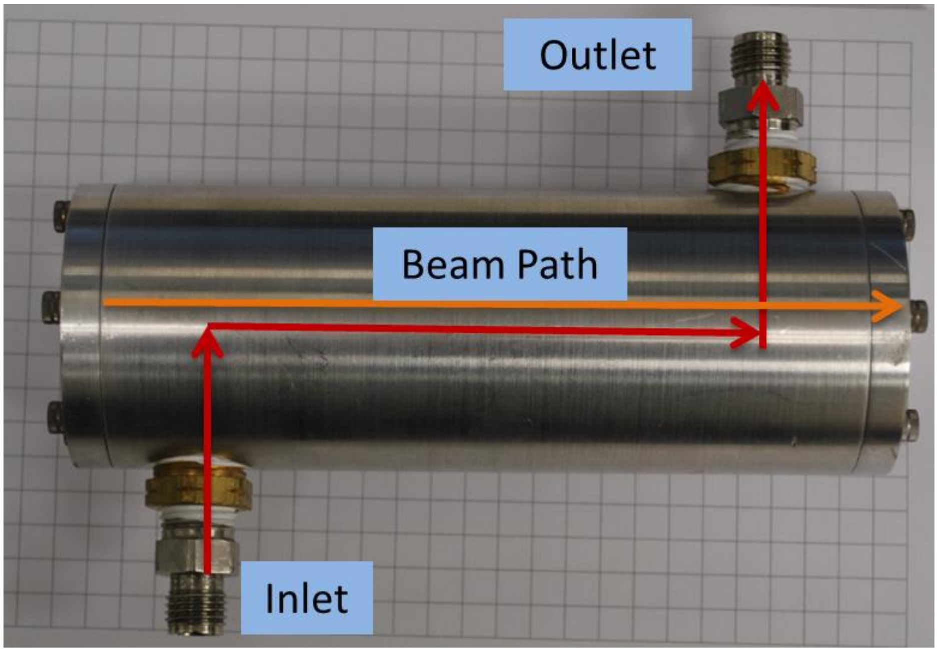

Figure 10: New cell design with coaxial optical and flow path to reduce regions of stagnation to improve cell time response.

The new coaxial design eliminates the stagnation regions presented in the old cell’s tee-shape design while maintaining a minimal volume. The new cell was outfitted with 10-mm diameter CaF_2 windows. Figure 11 highlights the improvements in decay time of the new absorption cell design.

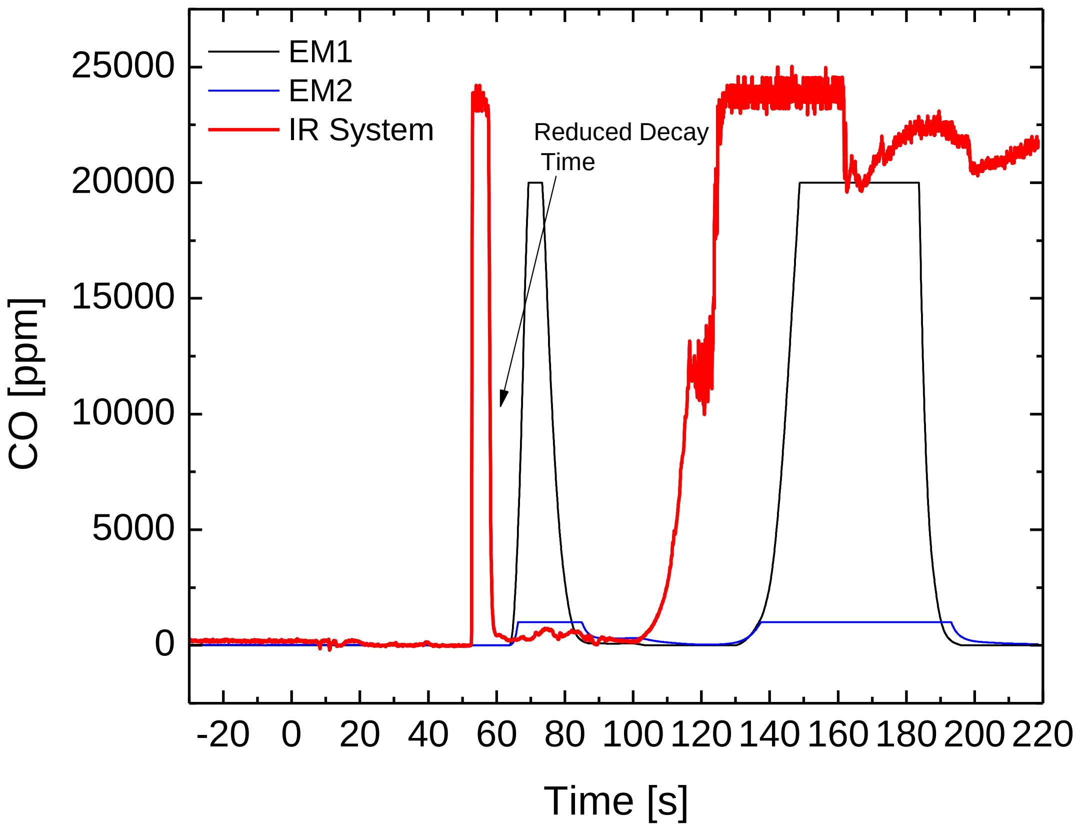

Figure 11: Reduced decay time in the IR system after installation of new absorption cell, as seen in run HF-01-02

The new cell showed a stark improvement in measurement response time and even allowed for greater resolution in features not resolved by EM1 and EM2. Figure 12 shows how the mid-IR diagnostic can resolve features not visible to the EM1 and EM2.

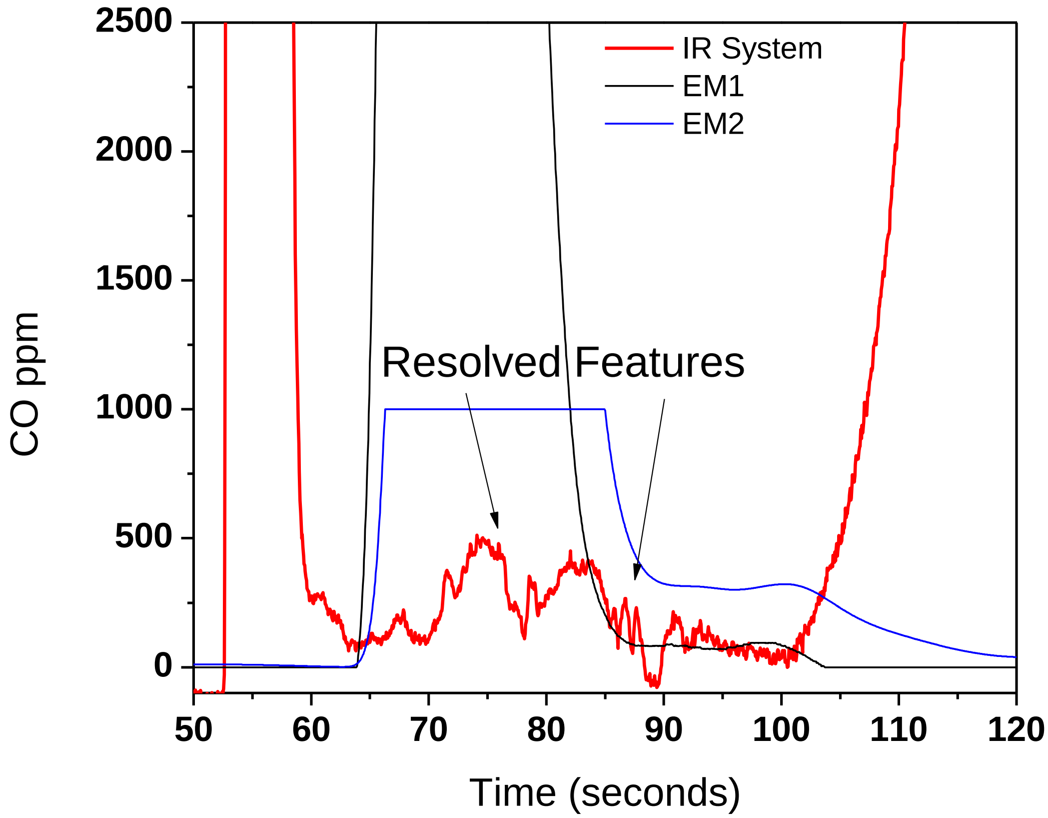

Figure 12: Better resolution of emissions features due to faster response time compared to EM1 and EM2

As testing continued, it became apparent that the amount of CO produced by the combustor rig was greater than what was previously predicted, and the mid-IR diagnostic had to be adjusted to accommodate higher CO values.

3.2.3 Short Cell

After conclusion of the first phase combustor test runs at the end of August 2015, it was found that both the mid-IR diagnostic developed by TAMU and the CAI CO analyzers were being over-ranged during combustor runs and had to be reconfigured to accommodate higher CO values. Figure 13 shows the saturation of all CO detectors.

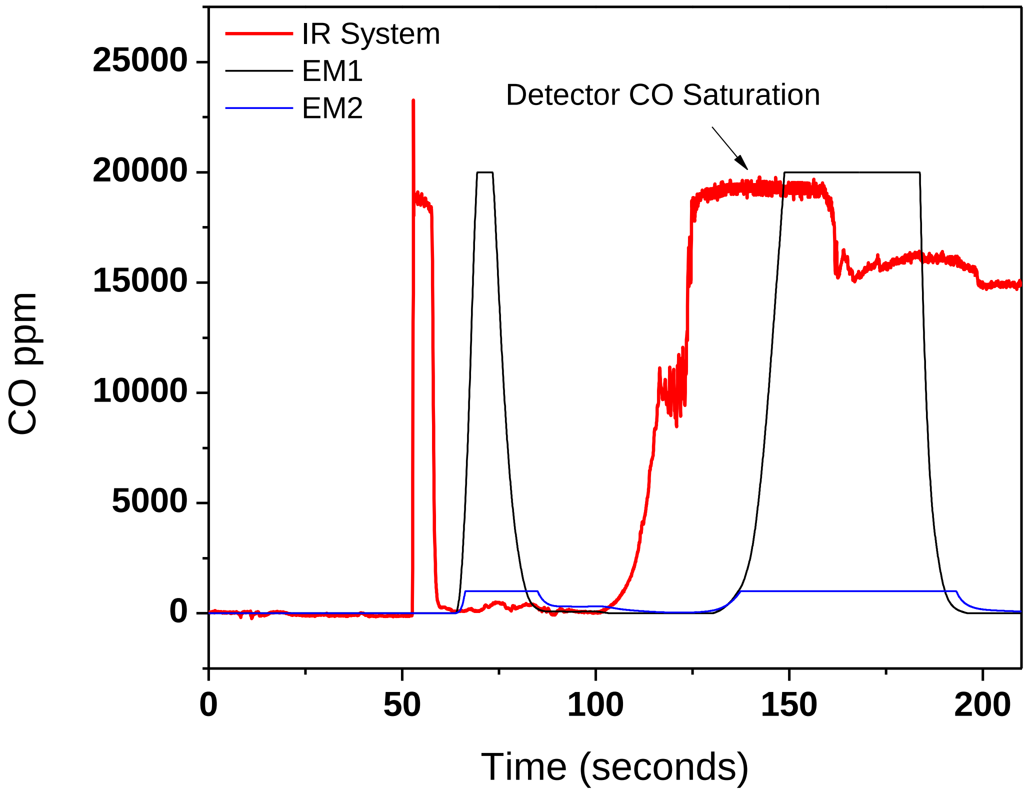

Figure 13: All CO diagnostics over ranged during the combustor transient occurring after 100 seconds

It was dictated by Toshiba that the new version of the diagnostic must be able to measure up to 5% CO (50,000 ppm). According to the Beer-Lambert law and spectral absorbance (Eqns. 23 and 24) the detectable mole fraction of the absorbing species has an inverse relationship to the distance the laser beam travels through the absorbing medium, meaning that to achieve a higher detection limit a shorter path length was needed. Figure 14 shows the laser absorption as a function of optical path length at the designated detection limit.

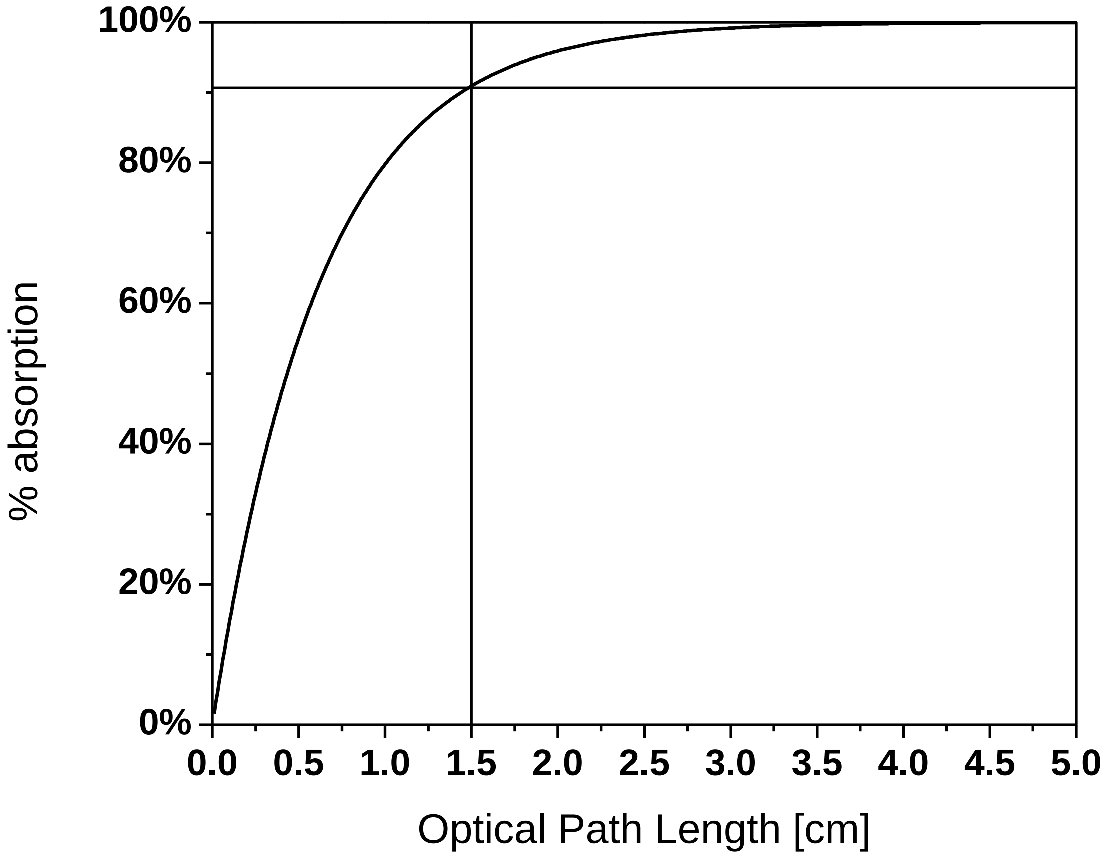

Figure 14: Laser absorption percentage vs optical path length for a gas at 300K, 1 atm, 5% CO by volume, K_v=32.

Figure 14 shows mole fraction as a function of path length for an absorption coefficient at normal test conditions. For an absorbance of 90%, it was found that an absorption path length of 1.5 cm would meet the stated detection requirement with the added benefit of further reducing the total cell volume for even better time response.

3.3 High-Pressure Combustor Rig

The combustor rig is a new facility that uses natural gas and an oxygen-carbon dioxide oxidizer mix to eventually provide low-cost electricity while eliminating nitrogen oxides and minimizing other pollutants. Figure 15 shows an image of the combustor on the test stand at the NTS facility. The combustor rig itself has an array of fuel and oxidizer flow subsystems, temperature and pressure sensors, and coolant systems to ensure stable operation. Inside the combustor is a Triethylaluminum-Triethylborane (TEA-TEB) injector for combustor ignition.

Figure 15: Side view of the Zeus combustor located at the NTS San Bernardino test site.

At the exit of the combustor rig is an emissions probe for collecting exhaust gas samples to be analyzed. Figure 16 shows a simplified schematic of the emissions probe mounted at the exit of the combustor. The housing of the probe is covered in a thermal coating while the probe itself is cooled by an internal flow of deionized water that exits near the tip of the probe insuring that the probe is not damaged by heat during combustor test runs.

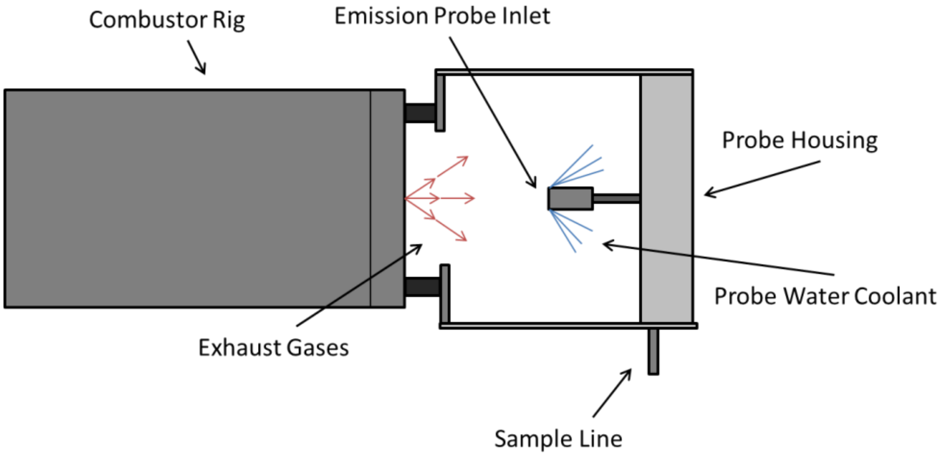

Figure 16: Diagram of the combustor rig and emissions probe mounted at the exhaust. The sample line provides the product gas sample that is sent to the CO-monitoring devices.

The probe is used to capture exhaust samples during test runs and feed the exhaust gasses to the emissions equipment housed in the emissions shed nearby. In the time it takes the exhaust gasses to flow from the emissions probe to the diagnostic shed, it is possible that the temperature of the exhaust gases will decrease to a value such that the vapor pressure of the water will fall below the partial pressure of the gaseous exhaust water, and water may begin to condense out of the exhaust. When measuring emissions, this causes issues due to not knowing exactly how much of the water is in gaseous or liquid form. To solve this issue for the CO laser absorption diagnostic, a heated line was installed that runs from the emissions probe to the emissions shed, ensuring that the measurement being made by the mid IR diagnostic was a wet measurement.

3.4 Other Diagnostics and Emissions Shed

As mentioned previously, other emissions equipment was used concurrently with the mid-IR diagnostic. The analyzer manufactured by CAI contained two separate CO analyzers; one was calibrated for measuring high levels of CO, while the other was calibrated for lower levels of CO. For the CAI analyzer to receive the sample exhaust, it first had to be passed through a conditioning system designed to remove water from the sample, ensuring no internal condensation within the analyzer and hence being able to assume a dry measurement. Inside the emissions shed was another exhaust analyzer designed by VIG Industries to measure the amount of unburned hydrocarbons (UHC). This quantity was a desired measurement because the amount of UHC is an indicator of incomplete combustion and inefficiencies within the combustor. Mounted within the emissions shed is a manifold used for distribution of calibration gasses and connections to the heated line leading to the emissions probe. Figure 17 shows a simplified schematic of how the combustor exhaust flows from the emissions probe to the emissions analyzers. Figure 18 is an image of the emissions shed from the combustor test stand.

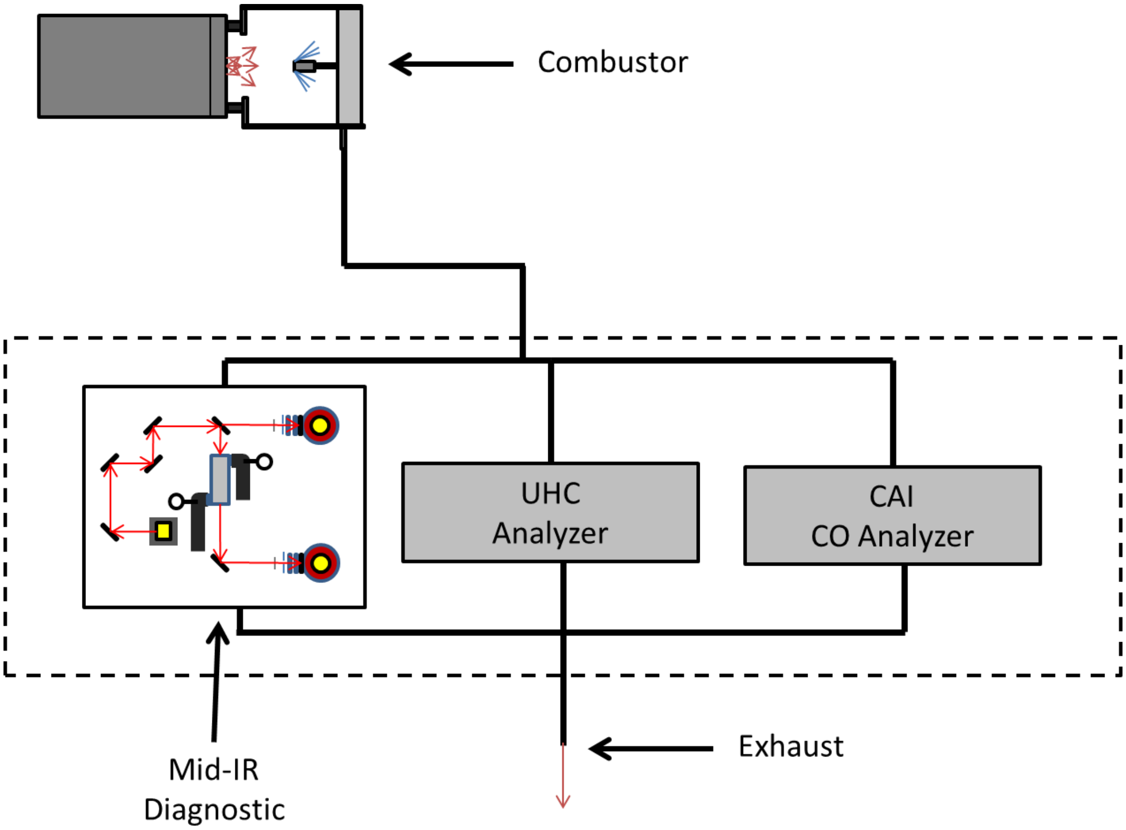

Figure 17: Simplified schematic of the exhaust flow to the emissions analyzers. The emissions shed housed all emissions equipment near the combustor test stand.

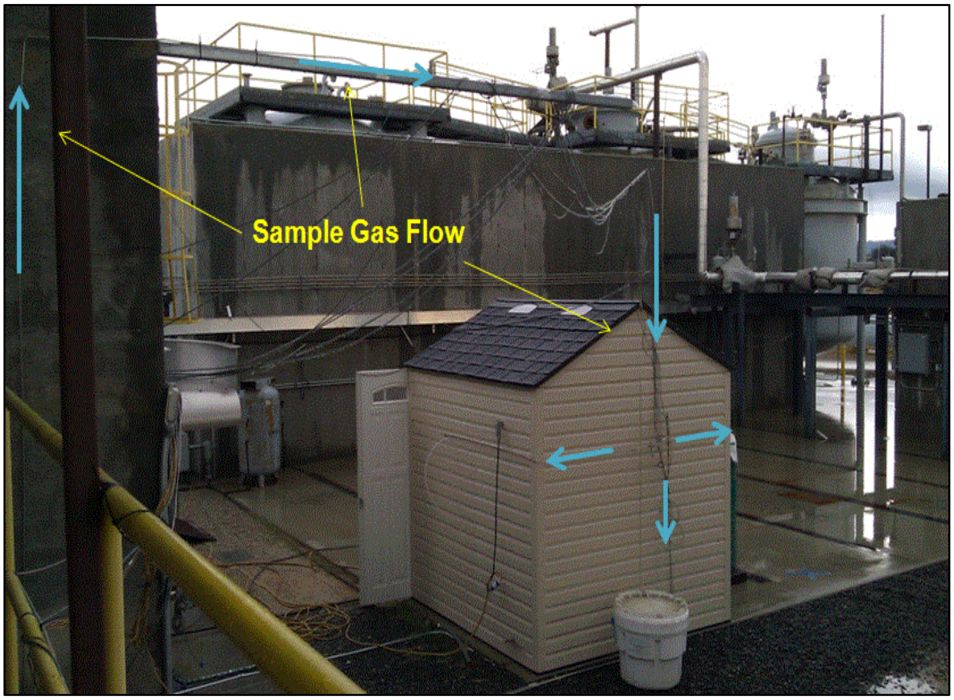

Figure 18: Image of the nearby emissions shed from the combustor test stand.

4. EXPERIMENTAL PROCEDURE

To ensure reliable functionality of diagnostic equipment when gathering reliable data, a set of calibration procedures was followed. The following sections discuss in detail the procedure used to calibrate the mid-IR diagnostic, validate that the QCL was operating at the designed wavelength, and to ensure proper voltage readings at the test facility's remote monitoring station.

4.1 Mid-IR Diagnostic Calibration

Prior to a combustor test run, and immediately after the run, a calibration procedure was conducted to determine the operational frequency of the QC and recorded using a portable oscilloscope located within the emissions shed. As mentioned in the experimental setup section, the InSb photodiodes are sensitive to environmental temperature, leading to a voltage offset referred to as the zero voltage. This voltage is recorded and subtracted from the recorded calibration signals during calibration analysis. In addition to the zero voltage, a baseline measurement must be recorded to determine the values of I_t and I_o prior to the introduction of a CO calibration gas. The cell is then evacuated and filled with a mixture of 4.04% CO by volume in a nitrogen balance, and the resultant signals and cell pressure are then recorded. Using the Beer-Lambert law and the measured parameters, the operational wavelength can be determined. The calibration procedure was also conducted after each run to determine any changes in laser operation.

4.2 Remote Data Acquisition System

Due to the relative proximity of the IR diagnostic to the combustor rig and the high-pressure, dangerous nature of the project, it was necessary for all diagnostic equipment signals to be relayed to the remote control center of the facility. All measured combustor parameters were monitored and recorded via LabVIEW at 20 samples per second. It was also necessary to record zero and baseline readings at the control center before and after each run, as it was discovered that the signal recorded within the emissions shed using an oscilloscope was not the same value as displayed in the remote control center. This discrepancy does not invalidate the calibration measurements, but just requires that a different set of zero and baseline measurements be recorded from the remote control center for combustor CO analysis. It should be mentioned that no personnel were allowed near the rig during a run (which could take several minutes including pre-test preparation, checkouts, etc.), so that the optical setup had to be robust enough to be stable during this entire time period.

5. DATA ANALYSIS PROCEDURE

After a combustor test run, all the data recorded in the control room with LabVIEW were given to PSI personnel for processing. PSI would then covert the LabVIEW data into an Excel file that displayed all the values of all pressure transducers, thermocouples, control valve voltages, and emission diagnostic outputs. The Excel file was then distributed pack to the PSI facility in Florida, the onsite Toshiba representative, and to the Texas A&M personnel. To quickly process the transmitted Excel document, a MatLab code was written to take all relevant diagnostic data, calculate an absorption coefficient, and solve the Beer-Lambert law for molar concentration of CO. To solve the concentration of CO passing through the mid-IR diagnostic, the absorption coefficient must be determined by calculating the absorption line strength and the Voigt profile at 2190.02 cm^{-1}.

The absorption line strength was determined by accessing the HITRAN database via the JavaHAWKS program. The HITRAN database contains spectroscopic data on many common gaseous species and can provide line strength data over a wide range of temperatures and wavelengths.[20] By using the HITRAN database and the thermocouple located at the inlet of the absorption cell, the CO line strength could be determined during any point in the run.

As mentioned in section 2.2.1, the Voigt profile is dependent on several parameters: temperature, pressure, concentration, and the collisional partners. While cell temperatures and pressures were directly measured, the concentrations of major collisional partners were estimated using equilibrium combustion chemistry. To determine the equilibrium species concentrations, the chemical kinetic suite Cantera was run utilizing the natural gas combustion mechanism GRI 3.0.[21] The analyses was performed at constant enthalpy and constant pressure and used the recorded temperature and pressure of the combustor at each recorded point in the run to generate a theoretical exhaust product profile assuming all species have had enough time to reach complete thermodynamic equilibrium. Figure 19 shows the exhaust products calculated using the GRI 3.0 mechanism.

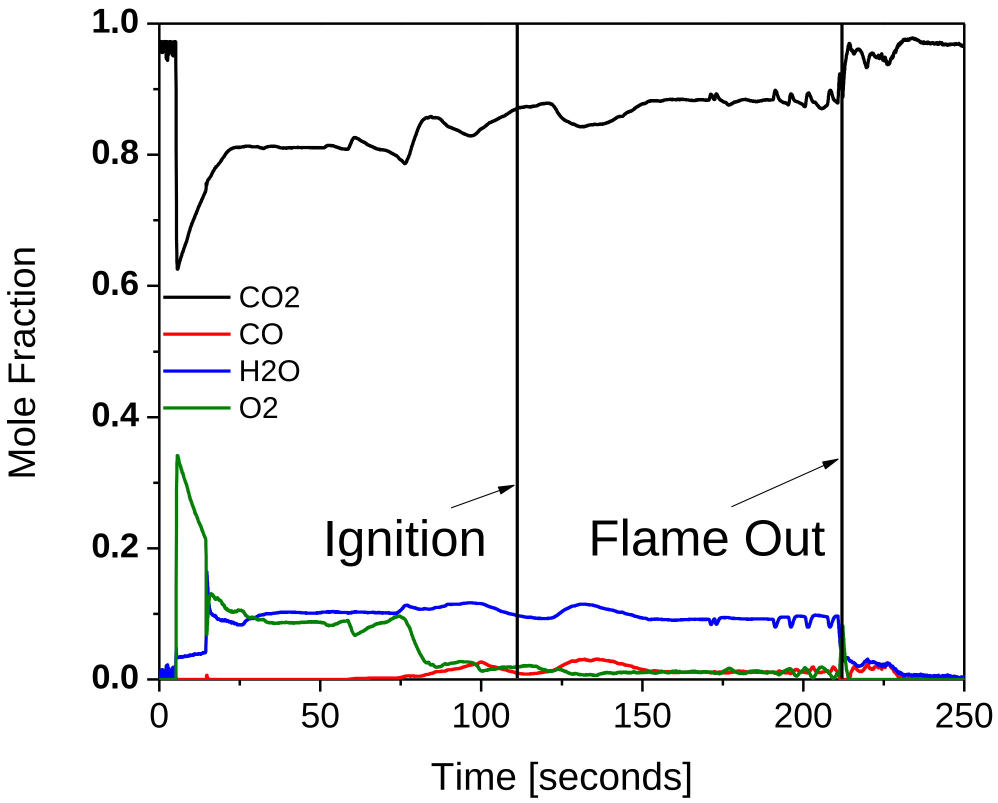

Figure 19: Theoretical emission output generated using the GRI 3.0 mechanism for a constant enthalpy, constant pressure reaction

The absorption coefficient was then determined for each point in the run using local absorption cell conditions, the calculated theoretical exhaust products, the operational wavelength of the QCL, the equations presented in 2.2.1, and a set of tabulated broadening coefficients, table 1, for H_2O, O_2, and CO_2. [22]

Collisional Partner	γ(300 K) (10^{-3} cm^{-1} atm^{-1})	n
CO-CO_2	65.6	0.54
CO-H_2O	127	0.78
CO-N_2	61.4	0.66
CO-O_2	50.1	0.60

Table 1: CO Line-broadening Parameters at 300 K for the $\boldsymbol{\nu'' = 0,}$ R(12) Transition of CO

After determining the absorption coefficient during each point in the run, the Beer-Lambert law was solved to generate a profile of the molar concentration of CO in the combustor exhaust. Figure 20 shows the absorbance of CO, $CO_{2,}$ and H_2O during the steady state region of a typical combustor test. The absorbance of CO compared to the absorbance of CO_2 and H_2O is magnitudes higher at normal test condition inside the absorption cell. This allows for the assumption that mid-IR diagnostic suffers no attenuation due to the presence of CO_2 and H_2O gases.

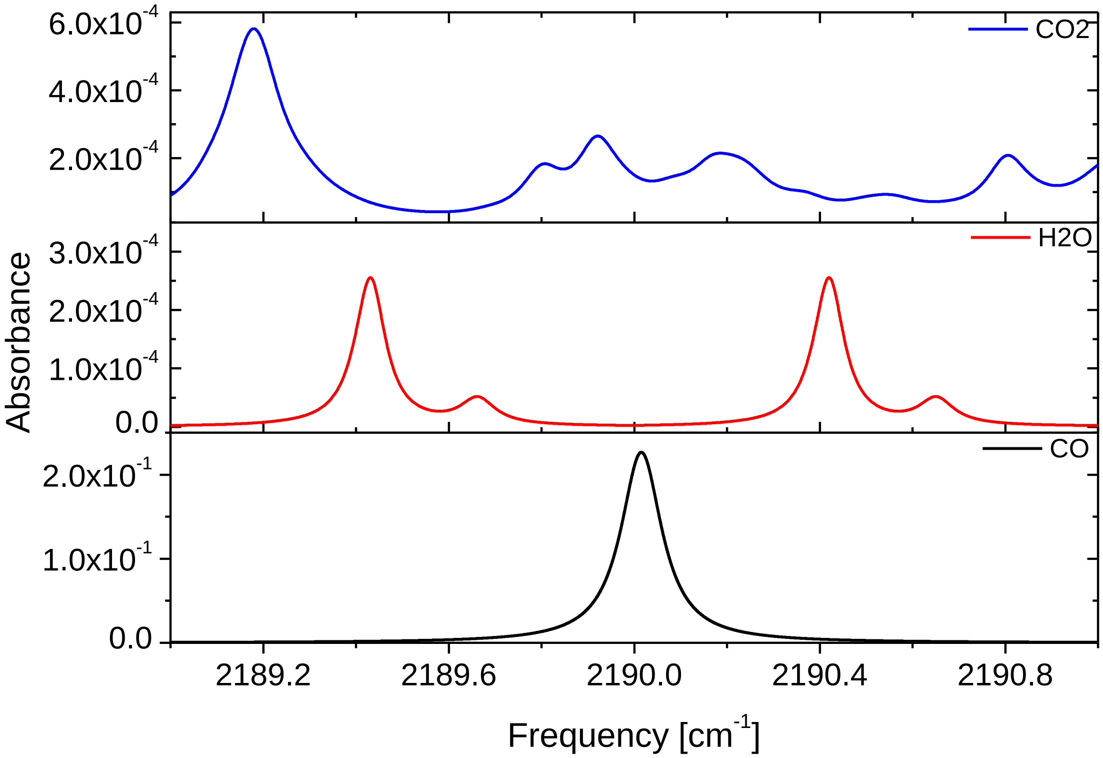

Figure 20: The absorbance of CO, CO_2, and H_2O at 380K, 0.85atm, absorption path length of 1.5cm, and mole fractions of CO, CO_2, and H_2O at 0.005, 0.895, and 0.10 respectively.

6. RESULTS AND DISCUSSION AND CONCLUSIONS

Over the course of the Zeus combustor project at the NTS facility, the design and layout of the mid-IR CO detector went through a series of improvements to meet the requirements of Toshiba and to make accurate CO measurements. As mentioned in section 3, the absorption cell was also refined to decrease residence times and to increase the detectable CO range. Combustor performance test have been occurring for several years starting in spring of 2013 and finishing November 3, 2015. After the conclusion of process 1, which demonstrated combustion functionality, process 2 was conducted, starting in September 2015, with the goal of reaching 26 set points. Because of other customers performing experiments at the NTS facility, and the time requirement in preparation for a combustor run, only 2-3 runs could be conducted in a day, but multiple points cold be reached in a single run. During process two a total of 35 experiments were attempted, with 5 aborted due to failed ignition, and 5 aborted due to triggering a redline condition. Not all of the planned set points were reached, but a significant number of points were achieved by the conclusion of process 2, enough to satisfy Toshiba.

6.1 CO Measurements During Combustor Performance Tests

A run that best demonstrates all improvements made to the mid-IR CO diagnostic was run SP2-HF-11 conducted on October 9, 2015. These data set show how the CO diagnostic has been improved to reduce the response time of the detector, increase the upper detection limit, and resolve emissions features not resolved by the other CAI gas analyzer. Figure 21 shows the improved response time and increased detection limit of the mid-IR diagnostic.

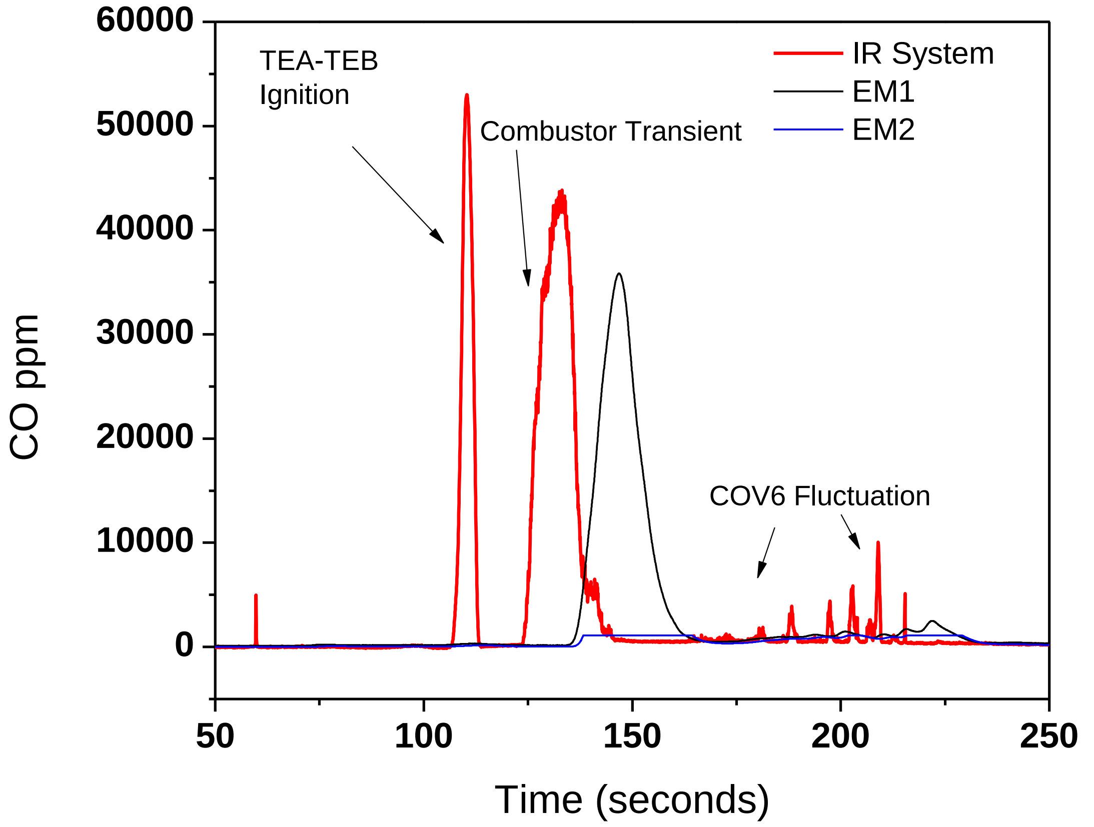

Figure 21: SP2-HF-11 CO Emissions Traces. The initial peak at approximately 105 seconds is due to the TEA-TEB ignition of the combustor. The second CO peak is due to the combustor entering a transient state to reach the test conditions. Fluctuations in the CO trace occur at approximately 175 seconds due to a malfunction in a CO_2 control valve.

The TEA-TEB ignition for SP2-HF-11 was not as robust as other combustor runs; as a result, the CO profile of the ignition was not as prominent. In Fig. 18, it is evident that while the ignition was weak, the CO profile was captured by the mid-IR system but was completely missed by the CAI gas analyzer. Other details of interest are that all mid-IR profiles were detected several seconds ahead of the other CAI CO detector. This reduced time delay was due primarily to the sample flow first having to pass through a sample conditioner before it reached the CAI analyzers, while the sample flows directly into the mid-IR detector from the emissions manifold. During the run, one of the CO_2 coolant flow valves (COV6) was experiencing a command and positioning issue. This issue caused the amount of CO_2 entering the combustor to fluctuate and thus alter the combustion chemistry, changing the amount of CO exiting the combustor. These fluctuation in the valve showed up as CO spikes in the data, as seen in better detail in the close-up plot in Fig. 22.

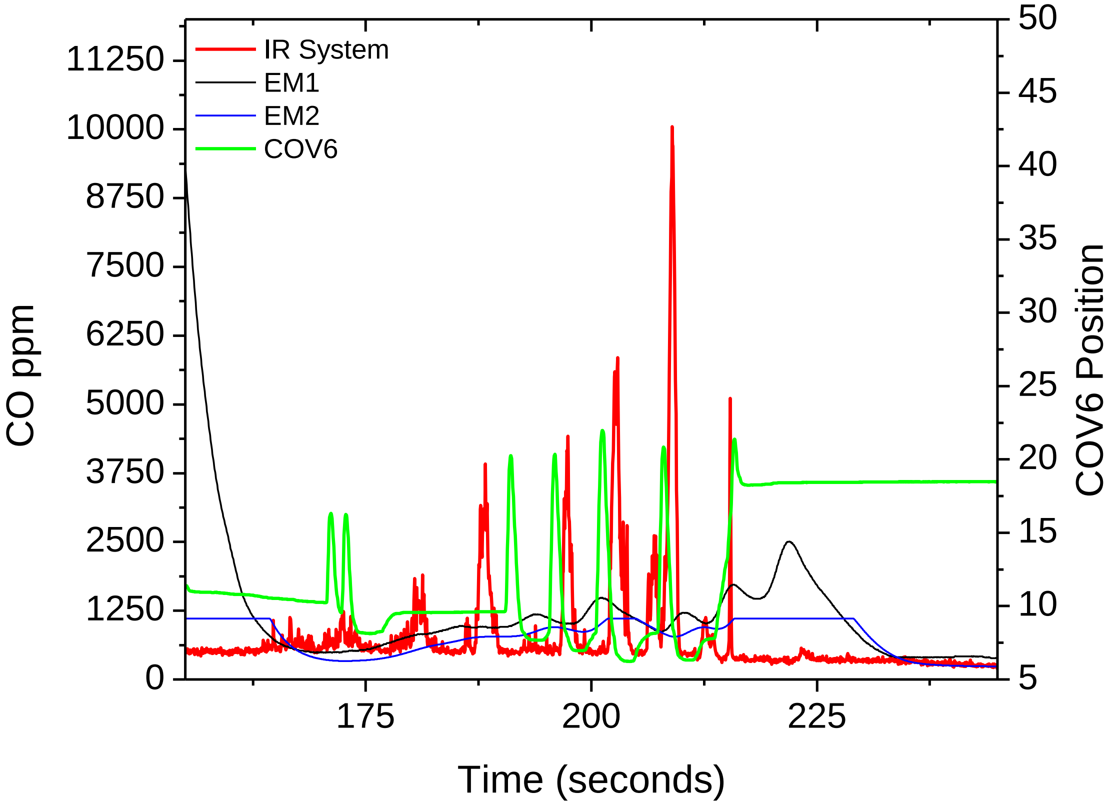

Figure 22: COV6 position trace showing the response time of the mid IR detector to fluctuating CO output (same as Fig. 18, but with close-up of fluctuating region).

It can be seen that fluctuations in COV6 had a direct correlation to CO output and that the mid-IR diagnostic was much faster and thus was able to resolve the features when compared to its CAI counterpart. Note that at about 190 seconds, the CO trace leads the COV6 change in position. While COV6 is can change the amount of coolant entering the combustor, it is one of many valves used to control the introduction of gases entering the combustion chamber and is not the only valve that can adjust the combustion chemistry. Figure 23 focuses on the steady state region at approximately 140 seconds.

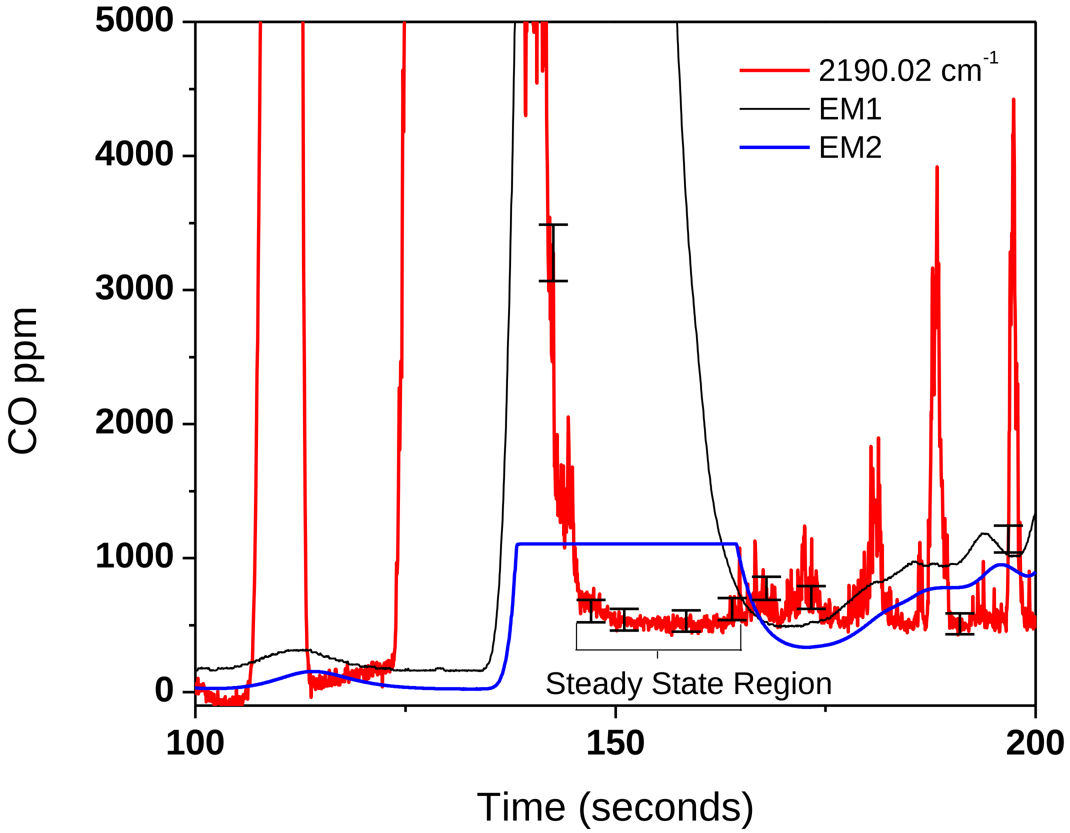

Figure 23: Stead state region of SP2-HF-11 occurring from 145 to 180 seconds

After the combustor has stabilized post ignition, it enters a transient phase to reach operational conditions. This transient is noted by a large spike of CO following the ignition spike. After the transient ramp, the combustor settles into the test region occurring at approximately 140 seconds for SP2-HF-11. During this time, the system reads about 539.5 ± 80.6 ppm CO. The uncertainty of the mole fraction was calculated using the Kline-McClintock method. For more information see appendix A1. The steady region lasted for approximately 35 seconds before the issue with COV6 caused the system to fall out of balance, and a combustor shutdown was triggered at 212 seconds.

An important improvement mentioned earlier was the installation of the heated line leading from the emissions probe to the emissions shed, causing the temperature of the flow entering the absorption cell to be well above the boiling point of water at 1 atm. Figure 24 shows the temperature and pressure inside the absorption cell during the combustor test. Figure 25 shows the theoretical H_2O partial pressure and the vapor pressure within the absorption cell during the run.

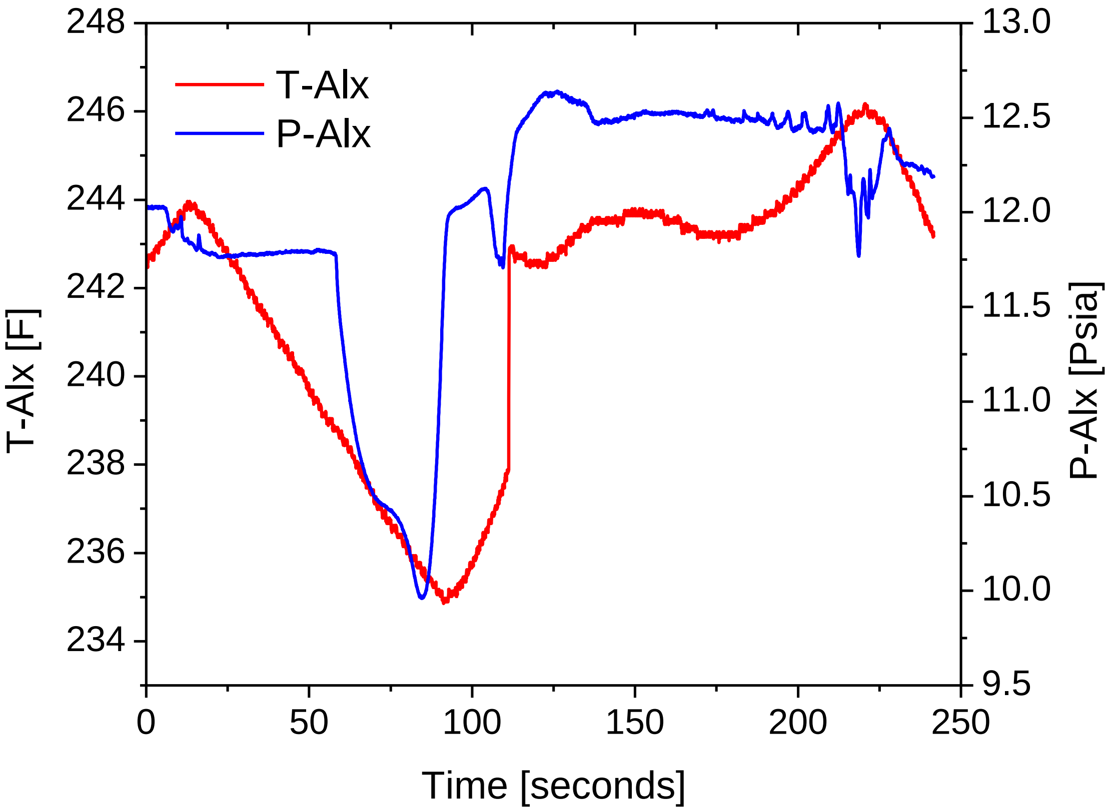

Figure 24: Absorption cell conditions for SP2-HF-11, T-Alx is the cell temperature, P-Alx is the cell pressure.

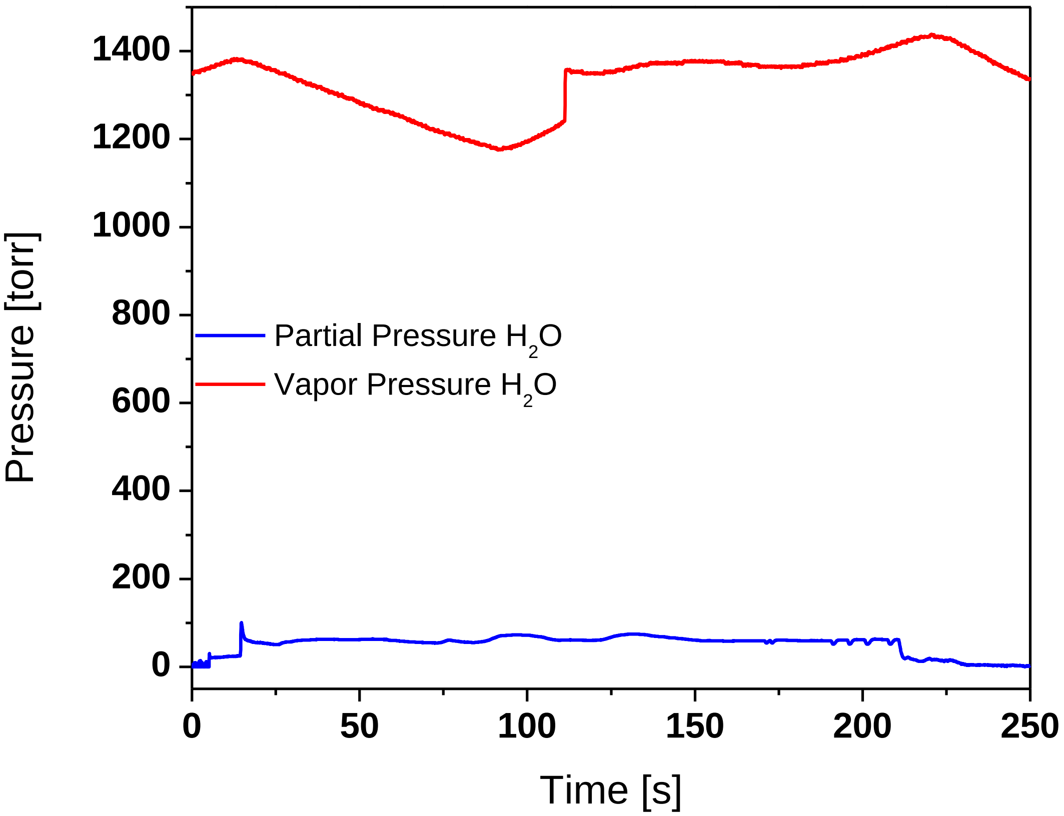

Figure 25: Theoretical H_2O partial pressure and the vapor pressure within the absorption cell for run SP2-HF-11.

This assurance that the water is in the gaseous phase reduces the error in measurement because it allows for the assumption of a 100% wet measurement when calculating the CO absorption coefficient.

Figure 26 shows the emission traces for SP2-HF-20, demonstrating a signal offset present at the end of the test for the mid-IR system.

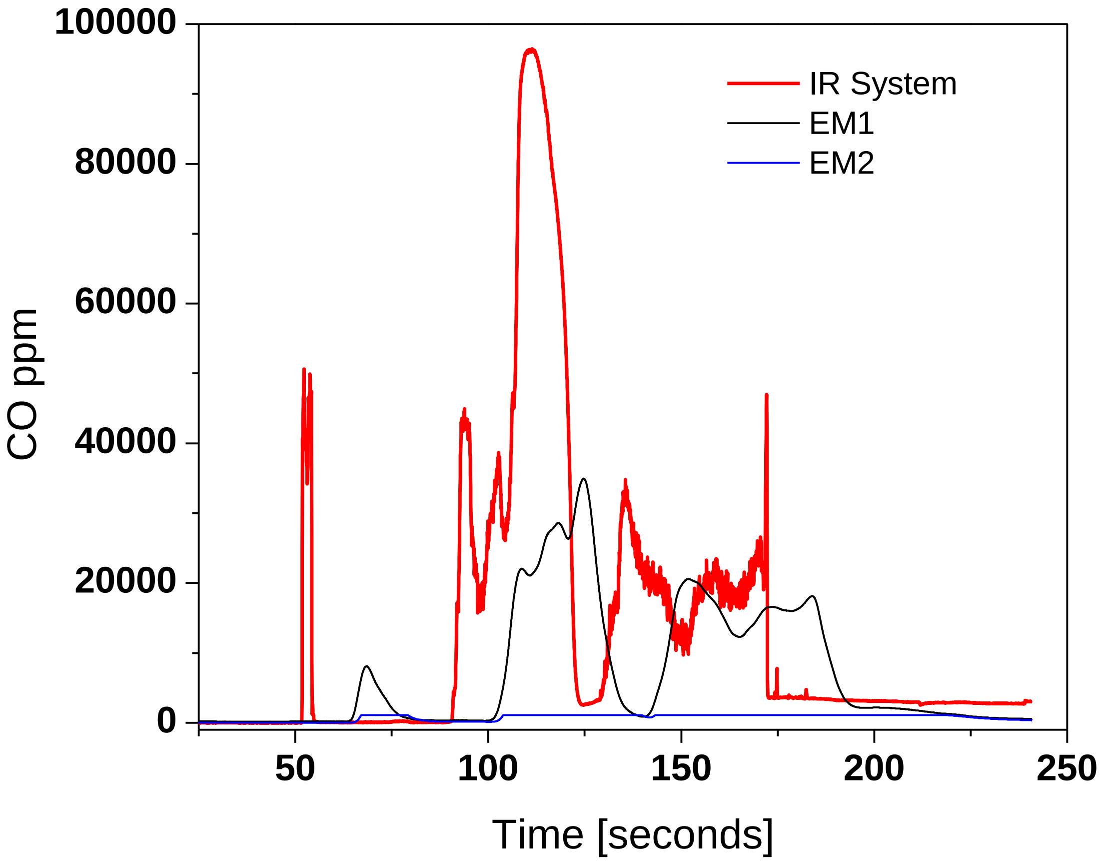

Figure 26: SP2-HF-20 ending CO reading levels off at 3000 ppm while EM1 and EM2 approach 0 ppm

One issue that was present in a minority of test runs was that the ending CO trace would not approach zero ppm after combustor flameout. This non-zero signal post-test can be caused by a number of issues due to the difficult environment in which the mid-IR diagnostic was operating. Figure 27 shows the raw voltage recorded from the InSb detectors during SP2-HF-20.

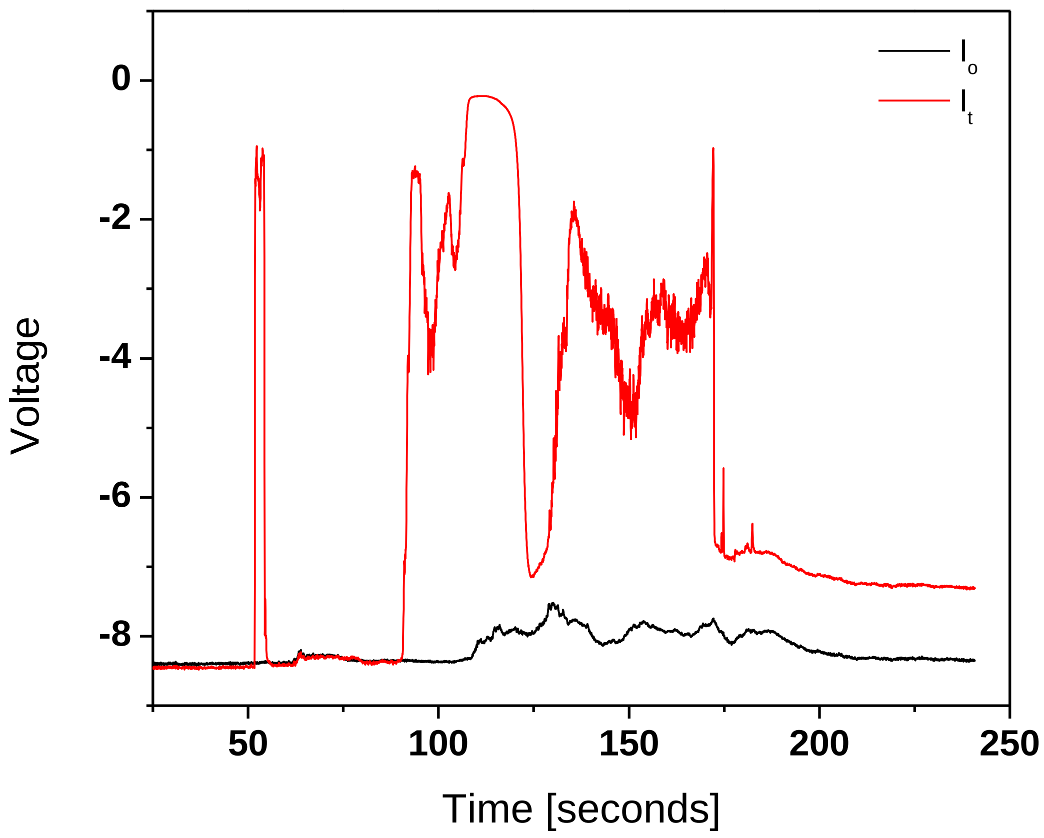

Figure 27: Raw voltage recording during SP2-HF-20

The starting voltage for both detectors in Fig. 24 is approximately -8.5 volts. The sharp rise at 50 seconds in I_t is due to combustor ignition, and the transient occurs at 80 seconds; but at 110 seconds, the laser appears to either become unstable or the optics table is undergoing mechanical vibrations due to its proximity to the combustor rig. Due to the symmetry of voltage oscillation patterns, it is more likely that the laser is undergoing mode-jumps that cause a shift in operating wavelength. This issue can generally be mitigated by the use of the reference and transmitted beams (I_o and I_t) to correct for changes in laser wavelength. It is visible that while the reference beam returns to the starting voltage after combustor flame out, the transmitted beam approaches -7 volts. As mentioned in section 4.1, a calibration of the mid-IR system was performed before and after each run to check for changes in the operational wavelength of the QCL. Figure 28 shows the results of the absorbance check of the diagnostic before and after the combustor run.

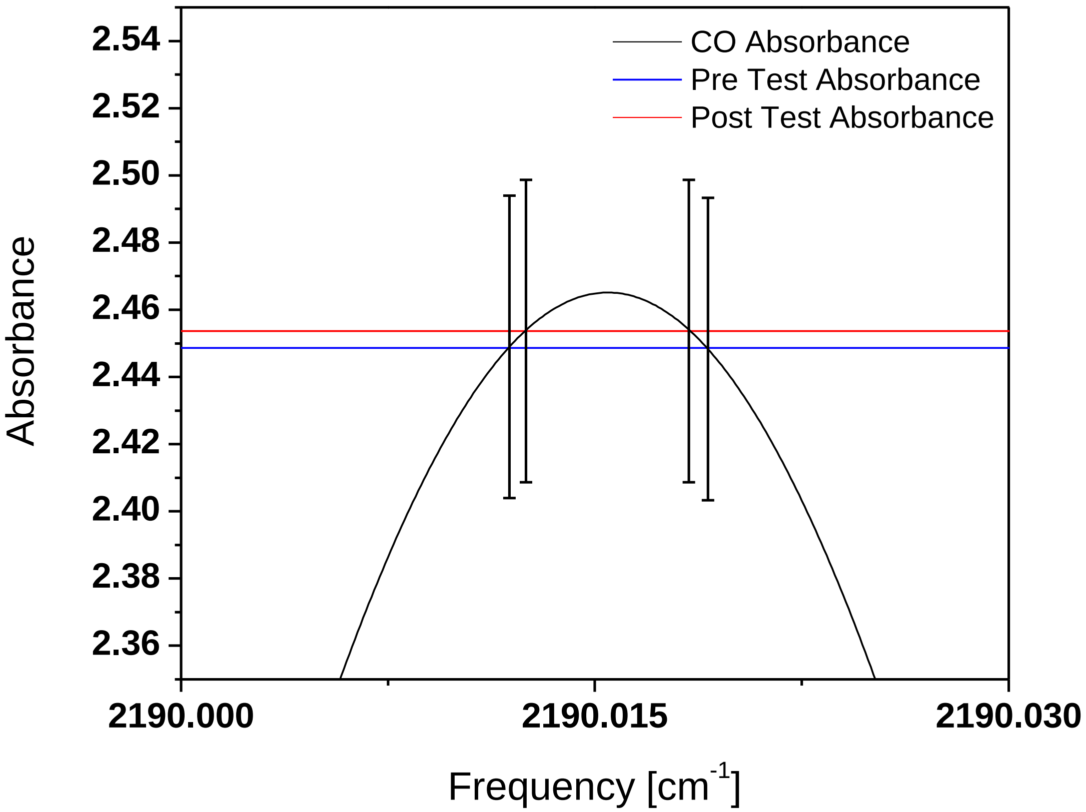

Figure 28: Absorbance check of the QCL for pre and post combustion test. Laser Line width is approximately 0.016 cm^{-1}.

The absorbance recorded from the calibration procedure shows a possible small change in operational wavelength, but was unlikely to be the sole cause of the voltage discrepancy.

Upon inspection of the absorption cell, it was discovered that a film of unknown composition and origin was deposited on the inner windows of the cell. This residue may be the cause of the diminished transmitted laser intensity while the operational wavelength of the laser remained the same. The source and composition of the deposited material is currently unknown. Figure 29 is a diagram of the cell windows before and after a combustor test.

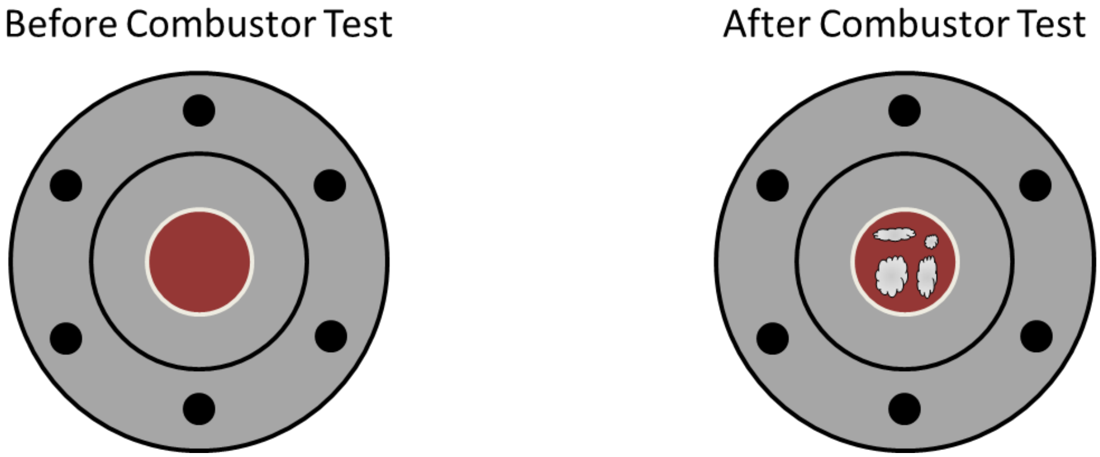

Figure 29: Depiction of absorption cell window ports before and after combustor test

7. RECOMMENDATIONS AND IMPROVEMENTS

Throughout the course of the Toshiba combustor test rig project, the environmental conditions in which the mid-IR CO detector was operating posted many challenges during the testing process. As mentioned previously, the CO detector was housed in a small shed near the combustor. A major difficulty when operating temperature-sensitive equipment is maintaining a constant environmental temperature throughout a set of measurements. Due to the location of the project and the housing arrangement of the equipment, it would be possible for the local temperature inside the shed to vary from 60°F all the way to at least 110°F throughout a day of testing during the summer months. This temperature extreme not only places stress on the QCL cooling systems, making stable laser conditions more difficult to manage, but it also caused the zero signal voltage of the InSb detectors to fluctuate dramatically throughout the day.

Another concern is mechanical vibrations of the system due to the proximity of the shed and optical table to the combustor rig. The above-mentioned difficulties could be mitigated by construction of a thermally and acoustically insulated structure located near the test stand. To ensure more preferable laboratory operating conditions, an air conditioner could be installed to keep the internal temperature of the structure low; also, the introduction of a floated optical table would drastically cut down on possible mechanical vibration effects. Another topic of interest would be the discovery of the source and mitigation of the unknown deposits on the cell windows that cause inaccuracies in CO measurement. One simple experiment would be to run a laser experiment off line to determine the timing and nature of the additional light extinction.

Finally, improvements in data reduction could be made in terms of a better understanding and measurement of collisional broadening parameters amongst the CO, CO_2, and H_2O species in the gas mixture.

REFERENCES

[1] Ren, W., Davidson, D. F., Hanson, R. K., and Farooq, A., 2012, "CO concentration and temperature sensor for combustion gases using quantum-cascade laser absorption near 4.7 μm," Applied Physics B: Lasers and Optics, pp. 1-12.

[2] Lin, X., Yu, X., Li, F., Zhang, S., Xin, J., and Chang, X., 2013, "CO concentration and temperature measurements in a shock tube for Martian mixtures by coupling OES and TDLAS," Applied Physics B: Lasers & Optics, 110(3), pp. 401-409.

[3] Chao, X., Jeffries, J., and Hanson, R., 2013, "Real-time, in situ, continuous monitoring of CO in a pulverized-coal-fired power plant with a 2.3 μm laser absorption sensor," Applied Physics B: Lasers & Optics, 110(3), pp. 359-365.

[4] Mihalcea, R. M., Baer, D. S., and Hanson, R. K., 1998, "A diode-laser absorption sensor system for combustion emission measurements," Measurement Science & Technology, 9(3), pp. 327-338.

[5] Barron-Jimenez, R., Caton, J. A., Anderson, T. N., Lucht, R. P., Walther, T., Roy, S., Brown, M. S., and Gord, J. R., 2006, "Application of a difference-frequency-mixing based diode-laser sensor for carbon monoxide detection in the 4.4–4.8 μm spectral region," Applied Physics B: Lasers & Optics, 85(2/3), pp. 185-197.

[6] Teichert, H., Fernholz, T., and Ebert, V., 2003, "Simultaneous in situ measurement of CO, H_2O, and gas temperatures in a full-sized coal-fired power plant by near-infrared diode lasers," Applied Optics, 42(12), pp. 2043-2051.

[7] Vanderover, J., and Oehlschlaeger, M. A., 2010, "A mid-infrared scanned-wavelength laser absorption sensor for carbon monoxide and temperature measurements from 900 to 4000 K," Applied Physics B: Lasers & Optics, 99(1/2), pp. 353-362.

[8] Ebert, V., Teichert, H., Strauch, P., Kolb, T., Seifert, H., and Wolfrum, J., 2005, "Sensitive in situ detection of CO and O_2 in a rotary kiln-based hazardous waste incinerator using 760nm and new 2.3μm diode lasers," Proceedings of the Combustion Institute, 30, pp. 1611-1618.

[9] Webber, M. E., Wang, J., Sanders, S. T., Baer, D. S., and Hanson, R. K., 2000, "In situ combustion measurements of CO, CO_2, H_2O and temperature using diode laser absorption sensors," Proceedings of the Combustion Institute, 28, pp. 407-413.

[10] Wang, Maiorov, Baer, Ds, Garbuzov, Dz, Connolly, Jc, Hanson, and Rk, 2000, "- In situ combustion measurements of CO with diode-laser absorption near 2.3 mu m," Applied Optics, 39(30), p. 11.

[11] Upschulte, B. L., Sonnenfroh, D. M., and Allen, M. G., 1999, "Measurements of CO, CO2, OH, and H2O in room-temperature and combustion gases by use of a broadly current-tuned multisection InGaAsP diode laser," Applied Optics, 38(9), pp. 1506-1512.

[12] Cassidy, D. T., and Bonnell, L. J., 1988, "Trace gas detection with short-external-cavity InGaAsP diode laser transmitter modules operating at 1.58 μm," Applied Optics, 27, pp. 2688-2693.

[13] Hanson, R. K., Kuntz, P. A., and Kruger, C. H., 1977, "High-resolution spectroscopy of combustion gases using a tunable ir diode laser," Applied Optics, 16(8), pp. 2045-2048.

[14] Camou, A., 2014, "Design and Development of a Mid-Infrared Carbon Monoxide Sensor for a High-Pressure Combustor Rig." Masters thesis, Texas A&M University, TX

[15] Turns, S. R., 2011, An introduction to combustion: concepts and applications. 3rd ed, Boston : WCB/McGraw-Hill, [2011]

[16] Eckbreth, A. C., 1996, Laser diagnostics for combustion temperature and species. 2nd ed, Amsterdam, The Netherlands : Gordon and Breach Publishers, [1996]
2nd ed.

[17] Anderson, J. D., Jr., 2006, Hypersonic and high-temperature gas dynamics. 2nd ed, Reston, Va. : American Institute of Aeronautics and Astronautics, [2006]
2nd ed.

[18] Hollas, J. M., 2003, Modern spectroscopy. 4th ed, Chichester : Wiley, 2003.
4th ed.

[19] Iwai, Y., Itoh, M., Morisawa, Y., Suzuki, S., Cusano, D., and Harris, M., 2015, "Development approach to the combustor of gas turbine for oxyfuel, supercritical CO_2 cycle," Turbine Technical Conference and Exposition GT2015 Montréal, Canada

[20] Rothman, L. S., Jacquemart, D., Barbe, A., Chris Benner, D., Birk, M., Brown, L. R., Carleer, M. R., Chackerian, J. C., Chance, K., Coudert, L. H., Dana, V., Devi, V. M., Flaud, J. M., Gamache, R. R., Goldman, A., Hartmann, J. M., Jucks, K. W., Maki, A. G., Mandin, J. Y., Massie, S. T., Orphal, J., Perrin, A., Rinsland, C. P., Smith, M. A. H., Tennyson, J., Tolchenov, R. N., Toth, R. A., Vander Auwera, J., Varanasi, P., and

Wagner, G., 2005, "The HITRAN 2004 molecular spectroscopic database," Journal of Quantitative Spectroscopy and Radiative Transfer, 96, pp. 139-204.

[21] Smith, G. P., Golden, D. M., Frenklach, M., Moriarty, N. W., Eiteneer, B., Goldenberg, M., Bowman, C. T., Hanson, R. K., Song, S., William C. Gardiner, J., Lissianski, V. V., and Qin, Z., http://www.me.berkeley.edu/gri_mech/

[22] Hartmann, J., Rosenmann, L., Perrin, M., and Taine, J., 1988, "Accurate Calculated Tabulations of CO Line Broadening by H_2O, N_2, O_2, and CO_2 in the 200-3000-K Temperature-Range," Applied Optics, 27(15), p. 3.

APPENDIX

A1. CO Concentration Uncertainty Analysis

Uncertainty analysis for the mid-IR analyzer was performed using the Kline-McClintock method. By manipulating the Beer-Lambert law, an expression for the molar concentration, A.1 can be derived. A.2 shows the uncertainty of the molar concentration (U_{X_i}). The uncertainty analysis depends on the partial derivatives of A.1 and is listed (A.3-A.7). Similarly the uncertainty of k_ν can be determined (A8-A13) by using the calibration data taken before and after the combustor runs. U_L was taken to be 0.01, U_P was take to be 0.02, $U_{I_t}$and $U_{I_o}$where taken to be 0.013, and U_{X_i} for determining U_{k_ν} was taken to be 0.02 as reported from the calibration gas supplier.

$$X_i = -\frac{1}{k_\nu PL}\ln\left(\frac{I_t}{I_o}\right) \tag{A.1}$$

$$U_{X_i} = \left[\left(\frac{\partial X_i}{\partial k_\nu}U_{k_\nu}\right)^2 + \left(\frac{\partial X_i}{\partial P}U_P\right)^2 + \left(\frac{\partial X_i}{\partial L}U_L\right)^2 + \left(\frac{\partial X_i}{\partial I_o}U_{I_o}\right)^2 + \left(\frac{\partial X_i}{\partial k_\nu}U_{I_t}\right)^2\right]^{\frac{1}{2}} \tag{A.2}$$

$$\frac{\partial X_i}{\partial k_\nu} = \frac{1}{k_\nu^2 PL}\ln\left(\frac{I_t}{I_o}\right) \tag{A.3}$$

$$\frac{\partial X_i}{\partial P} = \frac{1}{k_\nu P^2 L}\ln\left(\frac{I_t}{I_o}\right) \tag{A.4}$$

$$\frac{\partial X_i}{\partial L} = \frac{1}{k_\nu L^2 P} \ln\left(\frac{I_t}{I_o}\right) \tag{A.5}$$

$$\frac{\partial X_i}{\partial I_o} = \frac{1}{I_o k_\nu P L} \tag{A.6}$$

$$\frac{\partial X_i}{\partial I_t} = -\frac{1}{I_t k_\nu P L} \tag{A.7}$$

$$k_\nu = \frac{\alpha_\nu}{X_i P L} \tag{A.8}$$

$$U_{k_\nu} = \left[\left(\frac{\partial k_\nu}{\partial \alpha_\nu} U_{\alpha_\nu}\right)^2 + \left(\frac{\partial k_\nu}{\partial X_i} U_{Xi}\right)^2 + \left(\frac{\partial k_\nu}{\partial P} U_P\right)^2 + \left(\frac{\partial k_\nu}{\partial L} U_L\right)^2\right]^{\frac{1}{2}} \tag{A.9}$$

$$\frac{\partial k_\nu}{\partial \alpha_\nu} = 1 \tag{A.10}$$

$$\frac{\partial k_\nu}{\partial X_i} = -\frac{\alpha_\nu}{X_i^2 P L} \tag{A.11}$$

$$\frac{\partial k_\nu}{\partial P} = \frac{\alpha_\nu}{X_i P^2 L} \tag{A.12}$$

$$\frac{\partial k_\nu}{\partial L} = \frac{\alpha_\nu}{X_i P L^2} \tag{A.13}$$